

# Quantitative Morphology of Galaxies Observed in the Ultraviolet

L.E. Kuchinski<sup>1</sup>, Barry F. Madore<sup>2,3</sup>, M. Trewhella<sup>1</sup>, W. L. Freedman<sup>2</sup>

Received \_\_\_\_\_; accepted \_\_\_\_\_

---

<sup>1</sup>Infrared Processing and Analysis Center, Caltech/JPL, Pasadena, CA 91125

<sup>2</sup>Observatories of the Carnegie Institute of Washington, Pasadena, CA 91101

<sup>3</sup>NASA/IPAC Extragalactic Database, Caltech, Pasadena, CA 91125

## ABSTRACT

We present a quantitative study of the far-ultraviolet (FUV) and optical morphology in 32 nearby galaxies and estimate the “morphological  $k$ -correction” expected if these objects were observed unevolved at high redshift. Using the common indices of central concentration ( $C$ ) and rotational asymmetry ( $A$ ) to quantify morphology, we consider independently two phenomena that give rise to this  $k$ -correction. Bandshifting, the decrease in rest-frame wavelength of light observed through optical filters, is explored by measuring these indices in several passbands for each galaxy, and it is found to be the primary driver of changes in  $C$  and  $A$ . In general, the optical trend found for decreasing  $C$  and increasing  $A$  when going to shorter wavelengths extends to the FUV. However, the patchy nature of recent star-formation in late-type galaxies, which is accentuated in the FUV, results in poor quantitative correspondence between morphologies determined in the optical and FUV.

We then artificially redshift our FUV images into the Hubble Deep Field (HDF) filters to simulate various cosmological distance effects such as surface brightness dimming and loss of spatial resolution. Hubble types of many galaxies in our sample are not readily identifiable at redshifts beyond  $z \sim 1$ , and the galaxies themselves are difficult to detect beyond  $z \sim 3$ . Because only features of the highest surface brightness remain visible at cosmological distances, the change in  $C$  and  $A$  between simulated high- $z$  galaxies and their unredshifted counterparts depends on whether their irregular features are primarily bright or faint. Our simulations suggest that  $k$ -corrections alone are indeed capable of producing the peculiar morphologies observed at high redshift; for example, several spirals have  $C$  and  $A$  indices typical of irregular/peculiar HDF objects viewed at  $z \geq 2$ . We briefly discuss some elements of a scheme to classify

rest-frame UV images, mergers, protogalaxies, and other objects for which classical Hubble types do not adequately encompass the existing morphology.

## 1. Introduction

The morphology of galaxies in local and distant populations provides clues about the physical processes that shaped these systems, either at the time of their formation or during their evolution over the age of the universe. In the framework of the traditional Hubble scheme, morphology has been correlated with a number of fundamental underlying physical properties (for a comprehensive review see Roberts & Haynes 1994 and references therein). Elliptical galaxies are dynamically hot systems supported by their velocity dispersions, while spiral (disk) galaxies are dynamically cold and rotationally supported (*e.g.* Kormendy 1982). Bulge-to-disk ratios reflect the relative importance of dynamically hot and cold populations (*e.g.* Kent 1986). The presence of a bar may imply secular evolution that builds spiral bulges or produces starbursts (Pfenniger & Norman 1990; Courteau, de Jong, & Broeils 1996). Galaxies with early types in the Hubble sequence tend to be more massive, more luminous, and have less gas and a lower present-day star formation rate than late-type systems (Roberts & Haynes). However, it is expected that the morphology of high-redshift galaxies could be quite different from that observed locally. Theoretical scenarios of structure formation in the universe predict a significant fraction of mergers and interacting systems at high redshift compared to the local population (*e.g.* Baugh, Cole, & Frenk 1996). By carefully comparing samples of nearby and distant objects, it may be possible to identify the characteristics of protogalaxies and young star-forming systems and understand the roles of monolithic collapse and mergers in shaping the galaxies of the current epoch.

There are two major drawbacks to using the Hubble scheme in studies of galaxy evolution from deep surveys: its subjective nature, and its lack of descriptive and discriminative power for the irregular, starbursting, and interacting systems that may be more prevalent at high redshift. Classification into Hubble types is based on qualitative

analysis of observable features in each galaxy, and it can thus differ from one observer to another. Multiple features are considered and weighted together, making it difficult to automate classification on the Hubble sequence and occasionally yielding internally contradictory suggestions of the type (*e.g.* bulge-to-disk ratio *vs.* winding of the spiral arms). In a comparison of classifications of  $\sim 800$  galaxies by six expert morphologists, Naim et al. (1995) find a dispersion in revised Hubble  $T$  index of  $\sigma \sim 1.8$ , where a change of 1.0 corresponds to the difference between, *e.g.* Sa and Sab. For peculiar galaxies, the level of agreement between different experts' classifications is substantially lower (Naim & Lahav 1997), and the Hubble scheme does not divide the peculiar systems into any further categories beyond division of the faint irregulars with no bulge or arms and the peculiar galaxies that may have tidal features, mergers, or other obvious disruptions. This ambiguity at the late end of the Hubble sequence is particularly problematic for surveys that probe evolution of the galaxy population because there is evidence of an apparent increase in the fraction of irregular/peculiar galaxies at high redshift (*e.g.* Brinchmann et al. 1998; Driver et al. 1998; Abraham et al. 1996a).

In recent years, renewed attention has focused on the quantitative classification of galaxies as an objective, automated measure of their properties and evolution. The emerging methods are, by design, easily applicable to the current generation of large CCD imaging surveys. Abraham et al. (1994) developed a numerical index for the central concentration ( $C$ ) of galaxies, following the Yerkes classification system of Morgan (1958) and the correlations between concentration and Hubble type presented by Okamura, Kodaira, & Watanabe (1984) and Doi, Fukugita, & Okamura (1993). These authors later (Abraham et al. 1996b) added a quantitative measure of galaxy asymmetry ( $A$ ) to form a two-part classification system that distinguishes between three bins: E/S0 galaxies, spirals, and irregular/peculiar systems. If data from different wavelengths are available, it is possible to further divide the latest type bin between the Hubble Irr types and mergers

using a correlation between color and asymmetry that is valid only for non-interacting galaxies (Conselice, Bershad, & Jangren 1999; Conselice 1997). An important step in the development of this scheme was the classification of local galaxies based on their optical images, which provides the “calibration” of  $C$  and  $A$  to Hubble Types (Abraham et al. 1996b; Brinchmann et al. 1998; Conselice et al. 1999). This  $A$ – $C$  classification system has been used to study the distribution of morphologies in the *Hubble Space Telescope* (*HST*) Medium Deep Survey (Abraham et al. 1996b), the Hubble Deep Field (HDF, Abraham et al. 1996a), the ground-based Canada–France Redshift Survey and Autofib/Low–Dispersion Survey Spectrograph Redshift Survey (Brinchmann et al. 1998), and *HST* NICMOS deep images (Teplitz et al. 1998). Division of the morphological data into redshift bins demonstrates the increase in apparently irregular/peculiar galaxies at high redshift (Brinchmann et al. 1998).

To study galaxy evolution, it is important to understand the behavior of  $C$  and  $A$  as a function of wavelength in the local population before applying these indices to a sample of objects observed at a range of redshifts (*i.e.* different look-back times). At long rest wavelengths, where stellar light is a good tracer of mass, low degrees of central concentration and symmetry reflect a lack of dynamical organization that may characterize either interacting systems or those in the process of formation. At shorter wavelengths, asymmetry and patchiness are more likely to highlight cases in which dust and/or recent localized star formation strongly influence the observed morphology. Thus it is not surprising that  $B$ –band images already show lower  $C$  and higher  $A$  than their  $R$ –band counterparts (Brinchmann et al. 1998; Conselice 1997). In light of the physically different regimes probed by optical and UV light, it is necessary to understand how this morphological trend extends to the UV to determine if simple quantitative  $k$ –corrections are feasible for the concentration and asymmetry indices.

Because the rest-frame far-ultraviolet (FUV) light of galaxies is redshifted into optical filters at  $z \sim 3$  and into near-infrared (NIR) ones at  $z \sim 10$ , the UV morphology of local galaxies provides an essential basis for interpreting images of high-redshift systems. However, this wavelength regime is inaccessible from the ground, and the availability of UV galaxy images obtained from rocket and orbital missions has been limited until quite recently (*e.g.* O'Connell 1997 and references therein). The existing data suggest that UV and optical morphology are not often well-coupled (*e.g.* O'Connell 1997; Marcum et al. 1997, 2000; Kuchinski et al. 2000, hereafter K00). Thus it is difficult to interpret the influence of bandshifting on observed differences between the optical characteristics of nearby galaxies and the recorded rest-frame UV appearance of distant ones. Compared to their optical classifications, spiral galaxies generally appear to have later Hubble types in the UV (O'Connell 1997; K00). Spiral arms and star-forming rings are more prominent in the UV than at optical wavelengths, while bulges and bars are much fainter, nearly invisible, in the UV (Waller et al. 1997; K00). The UV radial profiles of disk galaxies are flatter than optical profiles, and the central concentration appears to be lower in the UV (O'Connell 1997; Fanelli et al. 1997a; K00). FUV images of late-type galaxies often appear much more fragmented than the optical view (O'Connell 1997), which raises the possibility of mistaking an ordinary irregular galaxy with a merging protogalaxy (see also K00). The effects of bandshifting on elliptical and S0 galaxies are less pronounced than on spirals: their FUV emission is smoothly distributed but is more centrally concentrated than optical light (O'Connell 1999). Although imaging distant galaxies in the infrared would lessen bandshifting effects by sampling the rest-frame optical instead of the UV out to  $z \sim 4$ , the rate of NIR data acquisition is currently slower than in the optical. Deep NIR imaging of small areas suggests that the increase in peculiarity may not necessarily be due to bandshifting (Bunker 1999), which could be confirmed more rapidly with large optical samples and a better understanding of the relationship between UV and optical

morphology.

In the absence of data, several attempts have been made to simulate the appearance of high-redshift galaxies by “extrapolating” the UV morphology from optical images or by applying the cosmological effects of surface brightness dimming and loss of spatial resolution. Artificial UV images of galaxies have been produced using template spectral energy distributions (SEDs) for different Hubble types to estimate the UV light in each pixel based on its optical colors (Abraham et al. 1996a; Abraham, Freedman, & Madore 1997; Brinchmann et al. 1998). The apparent change in morphology due to bandshifting in the *A–C* classification system has been quantified by Brinchmann et al. (1998) using this approach. They find that 13% of spirals are mislabeled as irregular/peculiar at  $z \sim 0.7$ , with the fraction rising to 24% at  $z \sim 0.9$ . This fraction may be expected to increase at higher redshifts as rest wavelengths move further into the UV. However, it is important to note that these simulations do not utilize actual UV data. The SEDs used to infer UV flux from  $B - R$  color may not accurately reflect local conditions, especially in very dusty regions or in localized starbursts (Donas, Milliard, & Laget 1995). Conselice et al. (1999) degrade the resolution and signal-to-noise (S/N) of optical images of nearby galaxies to simulate other effects of distance and redshift. They find their technique for measuring asymmetry to be robust to S/N variations (for  $S/N > 100$ ) but to show an apparent drop in the asymmetry index as spatial resolution decreases. Working with UV data directly to avoid uncertainties in the morphological  $k$ -correction due to bandshifting, Giavalisco et al. (1996a) and Hibbard & Vacca (1997) rebinned images and scaled the surface brightness to simulate redshifting. Their qualitative analysis of the resulting morphology suggests that even in the absence of bandshifting, cosmological effects cause the “redshifted” galaxies to have a later type and more irregular appearance (Giavalisco et al. 1996, Hibbard & Vacca 1997). However, without objective criteria to describe morphology, it is difficult to determine whether the magnitude of this effect is sufficient to account for the observed



increase in irregular galaxies at high redshift. Gardner et al. (1997) have measured the central concentration and asymmetry of five nearby galaxies on UV images resampled to simulate *HST* images at redshifts near  $z \sim 2$ , but the effects of surface brightness dimming were not considered. They also find that spirals tend to move to a later type bin in the *A–C* classification system. A quantitative study of the change in apparent morphology of local galaxies when viewed at high redshift is still necessary to determine how the distant galaxy population differs from that of the current epoch.

In order to compare the morphologies of galaxies at UV and optical wavelengths, we observed a set of 32 nearby galaxies in the FUV using the Ultraviolet Imaging Telescope (UIT) in low-earth orbit aboard the Space Shuttle Endeavour. In K00, we present FUV and ground-based optical data for these galaxies and discussed the morphology qualitatively based on images and surface brightness profiles. We find that localized star formation features dominate the FUV light and FUV–optical color profiles, in contrast to the smooth underlying distributions seen in optical images and profiles. The strong deviations from a smooth disk or disk + bulge profile that are evident in the FUV highlight the difficulty of determining traditional structural parameters from rest-frame UV images and suggest a need to move beyond the Hubble sequence to describe UV galaxy morphology.

In this paper, we present a quantitative analysis of the morphology of the K00 galaxy sample. We use central concentration and asymmetry parameters to quantify bandshifting and cosmological effects that are inherent in the study of high-redshift galaxies. This work extends the qualitative investigations of cosmological effects on UV images carried out by Giavalisco et al. (1996a) and Hibbard & Vacca (1997). Unlike the Brinchmann et al. (1998) study of redshift effects on morphology, we do not rely on the “extrapolation” of UV morphology from optical images. Section 2 reviews the sample selection and data acquisition and reduction, most of which is discussed in detail in K00. In Section 3, we present

our method for measuring the central concentration and asymmetry. The procedure for artificially redshifting images to take into account dimming and reduced spatial resolution is presented in Section 4, along with a qualitative discussion of these effects on apparent morphology. Section 5 contains the results of the quantitative morphology analysis and a discussion of the total morphological  $k$ -correction for  $C$  and  $A$  between local optical data and high-redshift galaxy images. In Section 6, we provide a brief summary, compare our artificially redshifted galaxies to deep HST images, and discuss implications for the study of high- $z$  galaxies. We also consider the shortcomings of both the Hubble scheme and the  $C$  and  $A$  indices for UV galaxy data, and we propose some new parameters that may more adequately describe the observed morphology.

## 2. The Data

### 2.1. Sample Selection

The morphological analysis in this paper was carried out on galaxies drawn from the sample of UV-optical data presented in K00, with the addition of a few galaxies for which there are UIT images but no optical data in our database. The sample selection for the UIT *Astro* – 2 mission, our source of UV galaxy images, is discussed in detail in K00. Although the UIT sample was designed to cover a range of morphologies from elliptical to irregular/peculiar, it does not statistically represent the local distribution of Hubble types. Because we wish to investigate in particular the morphology of the irregular faint galaxies seen at high redshift, our sample is weighted towards the spiral and irregular UIT galaxies. Different subsets of the sample are used for various parts of our study: only galaxies that fit entirely on the optical data frames and do not suffer central saturation in the optical filters are used to probe the behavior of apparent morphology with wavelength, and only galaxies that are still detectable in the FUV after artificial redshifting are used for the study

of redshift-dependent effects. We also artificially redshifted the  $U$ -band images of some galaxies into longer wavelength optical filters to study the effects of moderate redshift; again only galaxies that fit entirely on the optical frame were used. Table 1 contains some basic data for each galaxy in the sample and denotes for which parts of our investigation they were used. More detailed information about most of these galaxies and our observational data is given in K00.

## 2.2. Observations and Data Reduction

FUV images were obtained using the UIT and underwent the standard pipeline processing (Stecker et al. 1997).  $U$ ,  $B$ ,  $V$ ,  $R$ , and  $I$  images were obtained over the past several years at Palomar Observatory, Las Campanas Observatory, and Cerro Tololo Inter-American Observatory. The CCD images were bias-subtracted, flatfielded, and combined (where necessary) using standard procedures in IRAF (Tody 1986, VISTA (Stover 1988), and CCDPACK in Starlink. Artifacts such as the “UIT stripe” and cosmic rays on the optical images were removed, and background sky levels were determined for each image. We transformed the coordinates of the optical images to the system of the FUV image for each galaxy, yielding a final scale of  $1.14''/\text{pixel}$ . The optical images were then smoothed to the UIT resolution of  $\sim 3''$ . Finally, we masked out all foreground stars in the optical data and interpolated over those regions of the image. Data reduction procedures are described in more detail in Kuchinski et al. (2000)

## 3. Concentration and Asymmetry Indices

We have chosen to use the central concentration and asymmetry indices as quantitative morphology parameters because they are conceptually simple and have been used in a

significant body of recent work, especially in the study of distant galaxies (see references in the Introduction). In general, galaxies with high degrees of central concentration and symmetry will have an ordered, regular appearance and those with low central concentration and large asymmetry will have an irregular or peculiar morphology. (Here we explicitly distinguish between the Hubble “Irregular” type that is simply an extension of the late-type spiral sequence and the generic “Peculiar” type that has merger or interaction signatures, or unusual features that do not correspond to any other Hubble types.) The combination of these two parameters, plotted as  $\log A$  vs.  $\log C$ , has been shown by Abraham et al. (1996b) to divide nearby (optically-classified) galaxies into three broad morphological bins corresponding to the Hubble sequence: elliptical/S0, spiral, and irregular/peculiar/merger. This provides a basis for understanding distant galaxies in terms of the well-studied (at optical wavelengths) local population. As noted in several instances below, the intrinsic patchiness and low signal-to-noise of the FUV images have posed special difficulties for the techniques typically used to measure  $C$  and  $A$ . We have therefore modified the definitions proposed by Abraham et al. (1994, 1996), while retaining the general idea of a correlation between high concentration plus symmetry and an ordered appearance. The effects of these modifications will be explored later in this section.

It is important to carefully define a galaxy’s position and aperture in which the concentration and asymmetry indices will be measured because these indices are known to be sensitive to the centering and aperture size (Teplitz et al. 1998; Conselice et al. 1999). Many authors define the aperture based on a threshold set at some small multiple of the measured sky noise, and then use intensity-weighted image moments to define an ellipse (*e.g.* Abraham et al. 1996b; Teplitz et al. 1998). Aperture centers are typically obtained by centroiding on the brightest pixel (Teplitz et al. 1998). However, the patchy appearance and prominence of star-forming regions in the FUV images poses some significant difficulties for using these techniques in an unmodified manner. Sigma-clipping often produces multiple

small regions within what visually appears to be the galaxy aperture. Spiral arms or large areas of star formation can in fact be brighter than the geometric center of the galaxy (as defined by the optical center or by the apparent center of an ellipse enclosing the galaxy). Here we have used the available optical data to our advantage in defining the apertures. (It should be noted that this would not usually be possible in analyzing high-redshift galaxies). Isophotal fits to outer parts of the longest wavelength galaxy image (usually  $R$  or  $I$ ; images of the same galaxy in both filters yield nearly identical results) determine the ellipticity and position angle of the aperture. The centroid of this long wavelength image is selected to be the fixed aperture center. These ellipse parameters are identical to those used in K00 for azimuthal averaging to obtain surface brightness profiles. The maximum aperture radius is the largest radius at which there is still detectable light above the noise in the FUV image, which was determined by visual inspection of the light profiles of K00. This procedure for aperture radius selection yields a slightly different limiting surface brightness for each galaxy (depending on  $S/N$ ), which will be considered below in our determination of uncertainties in  $C$  and  $A$ . As a control, we use the same aperture for each filter’s image of a galaxy to ensure that we compare the same physical region of that galaxy at all wavelengths. For the small number of galaxies for which we have only FUV data, we estimate the center and determine the ellipse parameters from isophotal fits to the FUV image. In all of these cases, the ellipticity agrees well with the  $RC3$  value (de Vaucouleurs et al. 1991), and these particular galaxies are regular enough that the center is fairly unambiguous. The ellipse parameters for each galaxy are given in Table 2. As in K00, the merger NGC 4038/9 is considered as a single system with a center determined from a segmented image, and the aperture for NGC 3227 also includes light from its companion NGC 3226.

The concentration index  $C$  is the fraction of total galaxy light that is emitted from the central region compared to the whole. In practice, different authors have measured  $C$  using a variety of definitions (Doi et al. 1993; Abraham et al. 1994; Naim, Ratnatunga, &

Griffiths 1997). We select a very simple expression:

$$C = \frac{\sum_{(i,j): R < 0.3R_{\max}} I(i,j)}{\sum_{(i,j): R < R_{\max}} I(i,j)} \quad (1)$$

where  $R_{\max}$  denotes the radius of the elliptical galaxy aperture selected as described above. The calculation of total flux in the inner and outer elliptical apertures is performed on background-subtracted galaxy images. The choice of what fraction of  $R_{\max}$  constitutes the central region is somewhat arbitrary; for convenience of comparison, we select the value of 0.3 that was adopted by Abraham et al. (1994) and used in most subsequent analyses of galaxy concentration by these and other workers. Noise in the images should not present a serious problem for our concentration index because it should be evenly divided between “positive” (above the sky) and “negative” (below the sky) and thus should cancel out within each aperture. Concentration indices for each galaxy at every available wavelength are given in Table 2.

The asymmetry index  $A$  is a measure of the  $180^\circ$  rotational symmetry of the galaxy. The basic mathematical definition is as follows:

$$A = \frac{\sum_{(i,j): R < R_{\max}} |I(i,j) - I_{\text{rot}}(i,j)|}{\sum_{(i,j): R < R_{\max}} I(i,j)} \quad (2)$$

where the original image is rotated  $180^\circ$  to get  $I_{\text{rot}}(i,j)$ . By taking the absolute value of the difference between the original and rotated images, one introduces a systematic error because the sky noise always contributes positive values. For galaxies with regular shapes, in which all pixels in the aperture contain galaxy light, this error is a small fraction of  $A$ . On FUV images, which have low signal-to-noise and are intrinsically patchy or fragmented, the noise may be significant. Abraham et al. (1996b) correct for the noise by subtracting from  $A$  the measured asymmetry of a patch of sky with identical size to the aperture; but we typically do not have enough sky on our galaxy frames to apply this corrective technique. Instead, we consider the sky noise in pixels that do contain galaxy light, and

we also explicitly take into account the fact that many pixels within the aperture do not contain any galaxy light. We approach the latter problem by summing over only those pixels with values above a threshold of  $1.5\sigma_{\text{sky}}$  above the background, rather than all pixels in the aperture, when using Equation (2) for  $A$ . For optical images, most or all of the pixels are used in the sum, while in the FUV, the fraction may be as low as 10%. To correct for sky noise in the pixels that *do* contain galaxy light (and thus are used in the sum), we measure the asymmetry in a patch of sky as large as we can find on the image, then renormalize it to the number of pixels actually used in the sum. This correction factor is then subtracted from the asymmetry determined for pixels above the threshold. Thus the noise-corrected expression for the asymmetry is given by:

$$A_{\text{corr}} = \frac{\sum_{(i,j): p(i,j) > n\sigma} |I(i,j) - I_{\text{rot}}(i,j)|}{\sum_{(i,j): p(i,j) > n\sigma} I(i,j)} - k_A \quad (3)$$

where  $p(i,j)$  is the pixel value at position  $(i,j)$ ,  $n\sigma$  is the threshold, and  $k_A = N_{\text{pix}} * A_{\text{sky,pix}}$ .  $N_{\text{pix}}$  is the number of pixels in the aperture with values above the threshold, and  $A_{\text{sky,pix}}$  is the asymmetry per pixel due to sky noise, calculated by dividing  $A$  of Equation (2) for a patch of sky by the area (in pixels) of the patch. Values of the correction term  $k_A$  range from  $\leq 0.03$  for optical data to 0.1–0.2 for FUV images ( $A$  itself ranges from 0 to 1). The galaxy asymmetry values calculated with this method are given in Table 2.

We estimate the uncertainty in  $C$  and  $A$  by considering two factors: measurement error and errors that arise from using apertures extending to different limiting surface brightnesses. To quantify the error in measurement, we use five galaxies common to our sample and the digital atlas of Frei et al. (1996). (A sixth galaxy, M63, was saturated in the Frei et al. images and was not used for the comparison.) We calculate  $C$  and  $A$  from both sets of images (ours and theirs) and find  $\sigma_C = 0.016$  and  $\sigma_A = 0.011$ . The limiting surface brightness on the FUV images, which was used to determine the aperture radius for measuring  $C$  and  $A$ , ranges from  $\sim 24 - 25$  mag arcsec $^{-2}$ . For nine galaxies with limiting

surface brightness  $\geq 24.5$  mag arcsec $^{-2}$ , we measured  $C$  and  $A$  in an aperture extending only to 24 mag arcsec $^{-2}$  and compared the values to those measured in the maximum aperture size. In this case, we find  $\sigma_C = 0.025$  and  $\sigma_A = 0.012$ . The direction of the changes in  $C$  and  $A$  as aperture radius increases depends on the detailed structure of the galaxy, but it is typical to find a larger concentration and a larger asymmetry in the larger aperture. Adding these (independent) errors in quadrature yields our final uncertainty estimates: 0.03 for  $C$  and 0.02 for  $A$ .

We have also used the Frei sample to explore the effect of using different mathematical definitions of the  $C$  and  $A$  indices. This sample was used by Abraham et al. (1996) to calibrate the  $A - C$  classification system, and their  $C$  and  $A$  indices for individual galaxies are tabulated. We first tested our ability to recover the Abraham et al. values by using *their* definitions of  $C$  and  $A$  to measure indices on the Frei sample. The results are encouraging: a mean difference in  $C$  of  $0.001 \pm 0.015(1\sigma)$  and in  $A$  of  $0.006 \pm 0.047$ , both in the sense of (our measurement – Abraham et al.). We then used *our* definitions of  $C$  and  $A$  on the Frei sample to quantify the systematic difference between the two methods. The measurement of  $C$  differs only in the aperture definition, and we find an offset of  $\Delta C(\text{ours} - \text{Abraham}) = 0.03 \pm 0.02$ . In spite of the very different methods used to measure  $A$ , the offset is still small:  $\Delta A(\text{ours} - \text{Abraham}) = 0.04 \pm 0.03$ . These offsets are small compared to the uncertainties that we have estimated above, and small with respect to the errors of  $\sim 0.07$  quoted by Abraham et al.<sup>4</sup> Our results suggest that it will be possible to

---

<sup>4</sup>We note that the scatter in our calculated offsets is somewhat small compared to the uncertainties: this is likely because we have used the same images as Abraham et al. did. The quoted uncertainties include a term that takes into account differences in limiting surface brightness for different galaxies, which will not be a factor in comparisons using the same image of the same galaxy.



utilize the Abraham et al.  $A - C$  classification scheme using our values of  $C$  and  $A$ , with the morphological bins adjusted by the calculated offsets where appropriate.

#### 4. Artificial Redshifting

In order to study the influence on morphology of cosmological effects associated with large look-back times, we have artificially redshifted galaxy images to values of  $z$  at which the rest-frame FUV filter bandpass would coincide with the four *HST* WFPC2 filters used to image the HDF (Williams et al. 1996). We simulate the HDF because it comprises the deepest observation of distant galaxies to date, and has been the subject of numerous studies of morphology at high redshift. The FUV rest wavelength ( $\sim 1500\text{\AA}$ ) is redshifted into the broad-band F300W filter at  $z \sim 1$ , the F450W filter at  $z \sim 2$ , the F606W filter at  $z \sim 3$ , and the F814W filter at  $z \sim 4$ . (The precise value of  $z$  depends on which FUV filter was used for the UIT imaging and may vary from the approximate redshift given by up to  $\pm 0.2$ ; details of the two FUV filters are given in K00.) Because there is at present a paucity of  $U$ -band images of nearby galaxies, we also explore the effects of moderate redshifts that move the  $U$ -band rest wavelength into the F606W filter at  $z \sim 0.6$  and into the F814W filter at  $z \sim 1.2$ . We emphasize that there is no need to estimate the effects of bandshifting in these simulations; we simply selected a redshift such that the rest wavelength is placed directly into the desired filter. For example, a high-redshift galaxy at  $z \sim 3$  observed with WFPC2 in the F606W filter is really being observed in its rest-frame FUV, and a moderate redshift galaxy at  $z \sim 0.6$  in F606W is really being observed in its rest-frame  $U$ -band. By comparing the artificially redshifted images to their unredshifted counterparts, we can isolate the effects of surface brightness dimming and loss of spatial resolution on apparent morphology. Although this method restricts our investigation to specific redshifts, we span the range of  $z \sim 0.6 - 4$  over which recent work has suggested intrinsic evolution in the

galaxy morphologies.

We follow the procedures outlined by Giavalisco et al. (1996a) to artificially redshift the galaxy images, using their Equations (2), (5), and (7) to determine the resampling factor and surface brightness scaling. A cosmology with  $\Omega = 1$  and  $q_0 = 0.5$  is assumed throughout, and we take  $H_0 = 75 \text{ km s}^{-1} \text{ Mpc}^{-1}$  (*e.g.* Ferrarese et al. 1999). Because this value of  $H_0$  was also used to estimate the distances to sample galaxies, both the rebinning and brightness scaling factors will be independent of  $H_0$ . The dependence on  $q_0$  is much more complex, but Giavalisco et al. test values of both 0.05 and 0.5 and find that galaxies are more easily detected with the higher  $q_0$ . Filter and detector characteristics that are input to these formulae are taken from Stecher et al. (1997) for the UIT and Williams et al. (1996), *The WFPC-2 Instrument Handbook* (Biretta 1996), and *The HST Data Handbook* (Voit 1997) for the HDF. Galaxy distances are from Tully (1988) and are given in Table 1 of K00. Instead of convolving the resulting images with the *HST* point spread function (PSF) as Giavalisco et al. have done, we choose the more simple method of smoothing with a circular Gaussian to match the PSF width of  $\sim 3$  pixels reported by Williams et al. This technique avoids the difficulty of simulating in detail the complex PSF that results from *HST* optics and the “drizzle” procedure used to combine HDF images. Our redshifted images were then scaled to the appropriate HDF exposure time for each filter, and a sky background and sky noise were added based on the HDF values reported in Williams et al. We accounted for foreground Galactic extinction (very small in most cases) by correcting the input image to zero extinction before redshifting, then adding the appropriate extinction for each filter after the artificial redshifting was completed. The *B*-band foreground extinctions for each galaxy are from Burstein & Heiles (1984), and the Galactic extinction law of Cardelli, Clayton, & Mathis (1989) was used to calculate extinctions at other wavelengths.

As galaxies are artificially redshifted to high  $z$ , their appearance can change dramatically simply due to the fading of low surface brightness features and simultaneous loss of spatial resolution. In some systems, only the bright regions may survive the effects of dimming. Observed at simulated  $z \sim 4$  in the F814W filter of the HDF, the Im galaxy NGC 4214 appears in Figure 1 as a compact, regular object. For other galaxies, such as the Scd M101 (also shown in Figure 1), only bright star-forming regions in the spiral arms are visible at high redshift; the nucleus is quickly lost below the detection threshold. The spatial distribution of these features gives the artificially redshifted images a patchy, fragmented appearance suggestive of a later type galaxy, or even multiple systems (see also Giavalisco et al. 1996a). Most of the E/S0 systems in our sample are either undetectable at high redshift or have shrunk to the appearance of point sources. This strongly suggests that source counts at high redshift will be affected by a lack of early-type galaxies unless these systems have evolved significantly. At lower redshifts ( $z \leq 1$ ), cosmological effects are mild and the simulated galaxies simply look like fainter, more smoothed versions of their local counterparts. Figure 2 shows the results for the Sbc galaxy M51, whose rest-frame  $U$ -band data has been redshifted into the WFPC2 F606W and F814W filters. The simulated F606W image looks a great deal like the original  $U$ -band image, but by  $z \sim 1.2$  in the F814W filter, the galaxy is beginning to look less regular as the faint inter-arm light falls below the detection threshold. It is clear from these images that surface brightness effects play a significant role in determining the apparent galaxy morphology, and thus that cosmological dimming cannot be neglected in an analysis of high-redshift objects.

In the next section we will attempt to quantify the effects of redshift on morphology using the concentration and asymmetry indices. We consider only those galaxies that are detected and resolved on the simulated high-redshift images. First,  $C$  and  $A$  were measured on the artificially redshifted images using the procedures described in Section 3 and a fixed “physical” aperture size (*i.e.* size in kpc on the galaxy). For these measurements we

select an aperture size on the artificially redshifted image, then scale it by the appropriate bin factor to determine its size on the unredshifted image. This procedure isolates the effects of surface brightness dimming and reduced spatial resolution by comparing the same physical region of the galaxy at different simulated redshifts. We then recalculated  $C$  and  $A$  using a method that mimics the procedure an observer might follow: adjusting the aperture size for each image by visual inspection to enclose only the detectable light. In this case, the physical aperture size varies based on the limiting surface brightness of each simulated image. The apertures selected for high redshifts are often smaller than the size expected from scaling a galaxy’s rest-frame aperture by the bin factor for that redshift. This comparison is less direct than the one in which aperture size is fixed, but it is more indicative of analysis techniques for deep surveys. Table 3 gives the  $C$  and  $A$  values for the artificially redshifted FUV and  $U$ -band images in which apertures were adjusted based on limiting surface brightness. Differences between these results and the values for a fixed aperture size are discussed in Section 5.3.

## 5. Quantitative Morphology Results

In this section we discuss the results of our quantitative morphology investigation. We first consider the effects of bandshifting alone by comparing the FUV and optical morphologies of the sample galaxies within a fixed aperture (Section 5.1). The effects of surface brightness dimming and loss of resolution at high redshift, which we shall refer to collectively as the “cosmological effects”, are then discussed in terms of a fixed physical aperture size for each galaxy, *i.e.* one that samples the same physical region on rest-frame and simulated-redshift images (Section 5.2). We then compare the fixed aperture results with those obtained by adjusting the aperture based on each image’s limiting surface brightness, as an observer would do with real data (Section 5.3). Finally, we combine the

bandshifting and cosmological effects to discuss the total “morphological  $k$ -correction” between the optical appearance of nearby galaxies and images of high-redshift systems (Section 5.4). In several of the plots of concentration and asymmetry indices that are presented in this section, galaxies are divided into four bins by Hubble type. Symbols for the different bins are explained in the figure captions. Note that not all galaxies have optical data in every filter; that is, a plot comparing the  $B$ -band and FUV morphologies will not necessarily include all of the same galaxies as one comparing  $R$ -band and FUV images.

### 5.1. Bandshifting

FUV values of the central concentration index ( $C$ ) are predominantly lower than those measured on optical images of the same galaxy. The left-hand panel of Figure 3 illustrates the behavior of  $C$  as a function of wavelength for ten representative galaxies in our sample; galaxy names are labeled to facilitate the discussion below. The change  $\Delta C = C_{\text{OPT}} - C_{\text{FUV}}$  is shown as a function of  $C_{\text{FUV}}$  for all galaxies in Figure 4. Galaxies with large increases in  $C$  from FUV to optical wavelengths, (*i.e.* large positive values of  $\Delta C$ ), such as NGC 1097 and NGC 1566, tend to be early to intermediate-type spirals whose prominent optical bulges are faint to invisible in the FUV (see also K00). This effect is enhanced in barred galaxies due to the dominance of red stars in the bar, as shown for the SBa galaxy NGC 1512 in Figure 5. The change in  $C$  is less dramatic for late-type spirals such as NGC 1313, M51, and M63. Galaxies with ongoing, widespread star formation often have similar  $C_{\text{OPT}}$  and  $C_{\text{FUV}}$  because the light in both spectral regimes is dominated by the young stars. These systems include the starburst NGC 3310 (Smith et al. 1996, also shown in Figure 5), and the irregulars NGC 4214<sup>5</sup> and NGC 4449, as well as the starburst + AGN

---

<sup>5</sup>Fanelli et al. (1997b) find a starbursting core superposed on a faint disk in NGC 4214; however, our aperture for  $C_{\text{OPT}}$  encloses only the region containing FUV light and thus does

NGC 1068 (Neff et al. 1994). These galaxies have a higher  $C_{\text{FUV}}$  than others in our sample (see Figure 3 for NGC 3310 and NGC 4214), suggesting that the concentration index may be useful as an indicator of starburst activity in the analysis of rest-frame FUV galaxy images. Conversely, the merger system NGC 4038/9 shares the starburst trait of similar  $C_{\text{FUV}}$  and  $C_{\text{OPT}}$ , but has uniformly low values of  $C$  corresponding to its peculiar morphology (Figure 3). The starburst galaxy NGC 5253 is a conspicuous counter-example to the trend toward lower  $C$  in the FUV. Its UV-bright, centrally concentrated starburst produces a very high  $C_{\text{FUV}}$ , while older stars surrounding the burst contribute significantly to the optical light and thus reduce the value of  $C_{\text{OPT}}$ . Overall, the change in  $C$  due to bandshifting ranges from near zero to a maximum of  $\sim 0.4$ , or up to 40% as  $C$  theoretically ranges from 0 to 1.

The asymmetry values  $A_{\text{FUV}}$  are consistently higher than  $A_{\text{OPT}}$ , with a marked trend towards larger  $\Delta A = A_{\text{OPT}} - A_{\text{FUV}}$  in galaxies that are very asymmetric in the FUV (see the right-hand panels of Figures 3 and 4). UV-bright circumnuclear star formation in a “broken ring” shape dominates the FUV light of several galaxies, including NGC 1097 (Figure 3), NGC 1512 (Figure 5), and NGC 3351. This produces large  $A_{\text{FUV}}$  values even though the galaxies appear symmetric in optical light. In others, such as NGC 925 and NGC 2403, the underlying diffuse disk light is invisible in the FUV, and patchy light from young stars dominates  $A_{\text{FUV}}$ . The merger system NGC 4038/9 stands out in Figure 3 due to its extremely high  $A$  at all wavelengths compared to the other sample galaxies. As was the case for the concentration index, the asymmetry indices of the global starburst NGC 3310 (see Figure 3) and the starburst + AGN NGC 1068 are not very dependent upon wavelength. With the exception of NGC 4038/9 (which is plotted to the far right as an asterisk but is excluded from the fitting procedure described below), the right-hand panels

---

not sample the disk.

of Figure 4 show a tight correlation between  $\Delta A$  and  $A_{\text{FUV}}$ . The diagonal lines in Figure 4 show linear least-square fits to the data; solid lines are the fits to data for each filter individually, and the dotted line is the fit to all data together. The two lines in each panel are nearly identical, so  $A_{\text{OPT}}$  can be predicted from  $A_{\text{FUV}}$  using the dotted-line relation:

$$\Delta A = A_{\text{OPT}} - A_{\text{FUV}} = -0.92(\pm 0.05) \times A_{\text{FUV}} + 0.12(\pm 0.02) \quad (4)$$

where the standard deviation of the residuals is  $\pm 0.07$ . The maximum value for  $\Delta A$  can be quite large, reaching  $\sim 0.7$  (70%) in some cases. We stress that this relation, while useful over the range of Hubble types in our sample of local galaxies, needs further testing of its validity, especially for the mergers and protogalaxies encountered at high redshift.

We find one particular galaxy, NGC 4736, that highlights the limitations of using  $C$  and  $A$  indices for morphological comparisons. FUV and  $V$ -band images of this galaxy are shown in the bottom panels of Figure 5. As can be seen in Figure 3, the values of  $C$  and  $A$  for NGC 4736 change very little with wavelength in spite of dramatic morphological differences between the FUV and optical images. A bright star-forming ring produces high concentration in the FUV, while a large bulge increases the optical value of  $C$ . Symmetry in the ring that dominates the FUV images yields a low value of  $A_{\text{FUV}}$ , while an equally regular disk and bulge shape are responsible for a low  $A_{\text{OPT}}$ . The prevalence of star-forming inner and circumnuclear rings in the FUV (K00 and references therein) suggests that cases such as NGC 4736 may not be uncommon, and thus that the use of  $C$  and  $A$  to compare rest-frame UV and optical images may not adequately describe the detailed effects of bandshifting.

We now come to the most interesting general point of this study. In marked contrast to the results for optical data, the FUV values of  $C$  and  $A$  fail to segregate galaxies in our sample into the broad morphological bins of the  $A - C$  classification system of Abraham et al. (1996b). Figure 6 shows both FUV and optical  $C$  and  $A$  for the sample galaxies on

the  $\log A$  vs.  $\log C$  diagram. The dashed lines in Figure 6 are the Abraham et al. (1996b) divisions into morphological bins, (shifted by the offsets between our values and theirs that were calculated in Section 3). Errors in  $\log C$  and  $\log A$  depend on the values of these indices (we simply propagate the uncertainties in  $C$  and  $A$ ) and are shown on representative locations of the two diagrams. For the most part, the optical data for our sample galaxies lie close to their expected locations on this diagram. Three notable exceptions are the irregular starburst galaxies lying near the border between E/S0 and spiral classes: NGC 4214, NGC 4449, and NGC 5253. Thus it seems that the Irr/Pec/Merger bin of Abraham et al. describes peculiar/merging galaxies in our sample (*i.e.* NGC 4038/9 and NGC 3226/7), but not the irregulars with centrally concentrated starbursts. In the case of the FUV data, it is clear from the lower panel of Figure 6 that a majority of galaxies have landed in the extreme Irr/Pec/Merger region and some have undergone counter-intuitive shifts in location compared to their optical classifications. The peculiar galaxy NGC 5253 shifts to the earliest type bin in the FUV because of its centrally concentrated and highly symmetric starburst. The irregular galaxies NGC 4214 and NGC 4449 remain on the boundary between E/S0 and spiral in both optical and FUV, contrary to the behavior of the latest type spirals that have migrated from the Spiral to the Irr/Pec/Merger bin in the FUV. Several early-type spirals are located in the upper left corner, with very low  $C$  and high  $A$ , where the asymmetry in each case is due to a feature that is enhanced in the FUV but is considered a small or secondary part of the optical morphology. The three most extreme examples are NGC 1097 and NGC 1512, whose asymmetric circumnuclear star formation regions dominate the FUV light, and NGC 2841, whose high inclination and dusty disk produce a “lopsided” appearance that is likely due to extinction. Our sample is not large enough to provide more than individual examples of the problems associated with classifying UV galaxies using  $C$  and  $A$ . However, the FUV data in Figure 6 do not appear to suggest any natural way to divide the  $\log A$  vs.  $\log C$  diagram that unambiguously maps



back to the canonical (optical) Hubble type.

## 5.2. Cosmological Distance Effects

Our redshift simulations suggest that the concentration index is fairly robust to distance-related effects out to  $z \sim 3$ , but it appears to have a slight tendency toward decreased  $C$  on high redshift images in the  $z \sim 4$  simulation. The left-hand panels of Figure 7 show histograms of  $\Delta C = (C_{\text{rest}} - C_{\text{redshifted}})$ , giving the difference between our original “rest-frame” images (in either the  $U$  or FUV band) and their artificially redshifted counterparts. We have selected a bin width of 0.10 for  $\Delta C$  and  $\Delta A$ , commensurate with the uncertainties estimated in Section 3. As noted at the beginning of this section,  $C$  is calculated in a fixed physical aperture that samples the same regions of the unredshifted and simulated high- $z$  images. The median value of  $\Delta C$  is  $\leq 0.01$  for  $z \leq 3$ , but rises to  $\sim 0.06$  for the  $z \sim 4$  simulation. The potentially significant role of surface brightness effects is demonstrated in the galaxies M101 and NGC 4258, which are the outliers with  $\Delta C \sim 0.2 - 0.3$  in the redshift simulations of rest-frame FUV data (note that these galaxies are not detected in the  $z \sim 4$  simulation). Star-forming regions in the outer parts of the spiral arms are brighter than the inner galaxy. While light from the central regions is still visible in the unredshifted image and thus contributes to the inner aperture of  $C_{\text{rest}}$ , it has virtually disappeared in the artificially redshifted images and thus is not evident in the measurement of  $C_{\text{redshifted}}$  (see Figure 1 for M101). Special instances such as NGC 4258 and M101 can exhibit changes in  $C$  of up to 30% due to cosmological effects, but overall, most galaxies in our restricted sample have  $\Delta C \leq 5\%$  for  $z \leq 3$ .

Cosmological distance effects appear to introduce added scatter in the measurements of  $A$  with no clear systematic drift to either larger or smaller values at high redshift. As shown in the right-hand panels of Figure 7, the scatter is larger for the intrinsically asymmetric

FUV images than for the  $U$ -band images, even when artificially redshifted to similar  $z$ . The scatter in  $A$  due to distance effects ranges from 4% ( $=1\sigma$  about the mean) at moderate redshifts of  $z \sim 0.6$  to 12% at a redshift of  $z \sim 4$ . A galaxy will exhibit  $A_{\text{rest}} > A_{\text{redshifted}}$  (*i.e.*  $\Delta A > 0$ ) if faint irregular features have faded away with distance and/or if the decrease in spatial resolution has blurred asymmetric features in the rest-frame image. Conversely, galaxies may appear to have a higher asymmetry at high redshift ( $\Delta A < 0$ ) if the brightest features are asymmetrically distributed star-forming regions or spiral arms that do not get blurred together with distance. Thus changes in the value of  $A$  at cosmological distances depend on the rest-frame morphology of each galaxy at a level of detail more complex than is usually considered in the simple Hubble type. This suggests that the sensitivity of  $A$  to distance effects will severely limit its usefulness in comparisons of the morphology of local and distant galaxy populations.

### 5.3. Aperture Effects

The difference between the values of  $C$  and  $A$  measured with fixed apertures and those obtained by adjusting the aperture size based on limiting surface brightness are typically quite small ( $<5\%$ ), as shown in the histograms of  $\Delta(C, A) = (C, A)_{\text{fixed}} - (C, A)_{\text{adjusted}}$  in Figure 8. The bin size is smaller than that used in Section 5.2 because we expect the uncertainties to be less: we are comparing measurements made on the *same* image with different limiting radii. The concentration index is more sensitive than the asymmetry to small changes in aperture radius, which is not unexpected because  $A$  is calculated from sigma-clipped images in which the faint outer regions of the galaxy are not sampled in either measurement. The left-hand panels of Figure 8 show some tendency for  $C_{\text{fixed}} < C_{\text{adjusted}}$ , especially in low-redshift simulations. Fixed apertures were selected on the fainter high- $z$  simulations and thus are smaller than adjusted ones for these images. This means that

less of the bright galaxy “core” falls within the inner aperture of the  $C$  measurement (see Equation 1 in Section 3). An extreme example of this effect produces  $\Delta C \sim -0.3$  for the FUV image of NGC 4736: the bright starburst ring falls outside  $0.3R_{\text{max, fixed}}$  but inside  $0.3R_{\text{max, adjusted}}$ . Bright star-forming regions near  $0.3R_{\text{max}}$  in the FUV images of NGC 4258 ( $\Delta C \sim -0.2$ ) and M101 ( $\Delta C \sim -0.1$ ) produce similar effects, which are enhanced for these galaxies by the large change in  $R_{\text{max}}$  between the fixed and adjusted aperture calculations. Such effects are less noticeable in the artificially redshifted data because discrete bright features are blurred by the decrease in spatial resolution. Values of  $\Delta A$  cluster around zero, with only a handful of galaxies exhibiting  $A_{\text{fixed}} < A_{\text{adjusted}}$  due to exclusion of asymmetric outer regions like spiral arms from the smaller fixed aperture. We note that there are no aperture effects in the  $z \sim 4$  simulations because they have the highest limiting surface brightness: the fixed apertures were selected on these images and thus are identical to the adjusted apertures. Thus our asymmetry index  $A$  is quite robust to aperture effects for the changes in  $R_{\text{max}}$  that occur as galaxies fade with redshift, but the concentration index  $C$  may change either slightly or radically for individual galaxies depending on the details of their light distributions.

#### 5.4. Morphological $k$ -corrections

We can combine the results of the previous investigations that isolated bandshifting, cosmological, and aperture effects to investigate the overall difference in observed optical morphology between a sample of nearby galaxies and one of high-redshift objects. We emphasize that we have not simulated the possibility of enhanced star-formation in galaxies at large look-back times, although our sample does contain some local starbursting systems. We simply describe the difference between a population of galaxies observed locally and that *same*, unevolved, population observed at high redshift, both in the optical part of

the spectrum. For this comparison we have considered only galaxies that have  $C$  and  $A$  measured in the optical and either the  $U$ -band or FUV artificial redshifting simulations. This comprises a total of 20 galaxies, five of which have no  $U$ -band data and two of which have no artificially redshifted FUV data (due to lack of detection after the surface brightness dimming). Qualitative examples of the overall morphological  $k$ -correction are given in Figure 9, which shows galaxies as they would be observed locally in the  $V$ -band and as they would appear at moderate and high redshifts in the HDF filters.

As shown in Sections 5.1–5.3, bandshifting effects dominate the “morphological  $k$ -corrections” for our quantitative indices, changing  $C$  by up to 40% and  $A$  by up to 70% compared to typical changes  $\leq 10\%$  for distance and aperture effects. Although  $\Delta A$  due to bandshifting is correlated with  $A_{\text{FUV}}$ , scatter introduced by distance effects hinders the ability to predict the value  $A$  that would be measured for a particular galaxy viewed at high redshift. The  $k$ -correction for  $C$  and  $A$  is presented via the  $\log A$  vs.  $\log C$  classification diagram in Figure 10. Optical measurements for each galaxy are shown in the top left panel, followed by rest-frame  $U$ -band data redshifted to  $z \sim 0.6$  and  $z \sim 1.2$ , then rest-frame FUV data redshifted to  $z \sim 2 - 4$ . Again, not all galaxies are shown on every panel due to differences in the availability of data. The data in Figure 10 show a clear trend: at each succeeding redshift, the bulk of the points move toward lower  $C$  and higher  $A$ . By  $z \sim 2$ , most of our sample galaxies lie in the Irregular/Peculiar/Merger region. Galaxies that do not follow this trend are those (already noted in Section 5.1) that have similar optical and FUV morphology due to their prominent starbursts: NGC 3310, and to a lesser degree NGC 4214 and NGC 4449. NGC 1068 retains a very high central concentration even at high redshift (rest-frame FUV) due to the starburst + AGN core. The “trajectories” of position changes with redshift in the  $\log A$  vs.  $\log C$  diagram are shown for several galaxies in Figure 11, emphasizing the difference between spirals with dramatic changes in morphology (*e.g.* NGC 1097) and starburst systems (*e.g.* NGC 4449) whose appearance

would be similar locally and at high redshift. Given this non-monotonic migration of data points with redshift, it is no longer possible to divide this diagram into bins by Hubble type. Many of the early-type (Sa-Sb) spirals have joined the “mergers” in the upper left-hand corner, while later-type spirals and Im galaxies are spread over the “early type” regions of higher  $C$  and lower  $A$ . These results suggest that new methods will be required to classify high-redshift galaxies: UV values of  $C$  and  $A$  are inadequate to infer the optical morphology because the spatial distribution of young massive stars that dominate the UV emission may or may not be correlated with that of older stars that dominate the optical light and its morphological appearance.

## 6. Summary and Discussion

We have used numerical parameters that individually describe the central concentration and the asymmetry of galaxies to intercompare their apparent morphology in the UV and optical and to quantify the effects of redshift on the appearance of distant stellar systems. Bandshifting and distance effects, including changes in the apparent galaxy aperture as the limiting surface brightness of the image varies, are each considered separately, then combined in an overall discussion of the “morphological  $k$ -correction” in the  $C$  and  $A$  indices. Unlike previous models of the behavior of  $C$  and  $A$  with redshift (*e.g.* Abraham et al. 1996b, Brinchmann et al. 1998), we do not need to extrapolate the UV galaxy image from optical data because we use direct FUV images from the UIT. The inherent patchiness of galaxies in the UV and the low signal-to-noise of our data required that we modify the traditional methods of determining  $C$  and  $A$ , which were developed for high signal-to-noise optical data (Abraham et al. 1996b). However, we note that *a*) results from the two methods are only slightly offset, with small scatter, and *b*) the comparison of  $C$  and  $A$  at different wavelengths and simulated redshifts is internally consistent as it was done using

the same method for all measurements.

We find that bandshifting effects dominate the morphological  $k$ -correction, while distance effects introduce small, mostly random changes in the concentration or asymmetry indices. While the FUV values of  $C$  and  $A$  generally show an extension of the optical trends (noted by Brinchmann et al. 1998) toward lower concentration and higher asymmetry at short wavelengths, they can be much larger in magnitude: up to 40% for  $C$  and 70% for  $A$ . Some counter-intuitive results are produced by the strong dependence of FUV morphology on current star-formation: circumnuclear rings in some early-type spirals, combined with the fading of the red bulge at UV wavelengths, produces the high  $A$  and low  $C$  which are usually associated with irregular/peculiar objects in spite of these galaxies' regular appearance in the optical. Centrally concentrated starbursts in some late-type and irregular galaxies can give them a more regular morphology in the FUV, with the high  $C$  and low  $A$  typical of E/S0 galaxies.

Our simulations of distance effects alone show that they tend to produce small changes (up to 7%) in  $C$  and slightly larger offsets (up to 12%) in  $A$ . These values are measured within a fixed physical aperture (in kpc) that samples the same region of the galaxy at each redshift. When the aperture size is varied to match the limiting surface brightness of individual images, additional scatter of  $\sim 3\%$  is found in our measurements of  $C$  and  $A$ . However, there are individual galaxies for which distance and aperture effects are particularly noticeable due to the location of extremely bright star-forming features well away from the galaxy center. These examples provide a cautionary note on the possibility of large excursions in the derived type due to distance effects.

In this paper, as well as in K00, we find that it is extremely difficult to unambiguously map a galaxy's FUV morphology to its optical Hubble type, or to the  $C$  and  $A$  indices in the optical that appear to be correlated with Hubble type. The images in K00 suggest that

most galaxies exhibit a later Hubble type in the FUV, but the magnitude of this shift, even in qualitative terms, is clearly much larger for some galaxies than for others. The same phenomenon is seen in the  $A - C$  classification system, for which a variety of morphological  $k$ -corrections are shown in Figure 11. We show in Figure 10 that the overall changes in  $C$  and  $A$  with redshift make it nearly impossible to use the classification system of Abraham et al. (1996) for rest-frame FUV data, or beyond  $z \sim 2$  in our simulations. Moreover, it is difficult to see how the three morphological bins based on optical Hubble type could be redrawn to accomodate the rest-frame FUV data. The location of UV galaxies on the  $\log C$ - $\log A$  diagram depends on details in the spatial pattern of star-formation (*e.g.* circumnuclear rings), which are not necessarily included in the simple Hubble type.

One of the nagging questions in the interpretation of peculiar morphologies in the HDF and other deep surveys is whether or not they are typical spiral or irregular galaxies viewed at high redshift (*e.g.* Bunker 1999). The best available comparison data for our simulated sample of galaxies at cosmological distances are the  $A$ - $C$  classifications of HDF galaxies presented by Abraham et al. (1996a). Figure 12 shows the loci on the  $\log A$  vs.  $\log C$  diagram for our redshifted simulations (points), the HDF morphologies from Abraham et al. (shaded polygon) and the local optical galaxy sample of Frei et al. (1996) artificially redshifted to  $z = 0.5 - 2.0$  by Abraham et al. (open polygon). The shaded and open polygons have been shifted from their loci in Abraham et al. by the offsets calculated in Section 3. Nearly all of our simulated data points for  $z \leq 1.2$  lie within the open polygon, which is the locus of non-evolving galaxies. The lack of points in the right-hand half of the polygon is due to the paucity of ellipticals in our sample. It is likely that our  $z \sim 2$  data lie outside the open polygon because the rest-frame FUV of our simulations is not analogous to the rest wavelength of the Abraham et al.  $z = 2$  simulation. Our artificial  $z \sim 2$  data are rest-frame 1500Å images viewed through the F450W filter, while Abraham et al. (1996a) use the F814W HDF images, which sample rest-frame  $\sim 2500$ Å at  $z \sim 2$ . (We have no data

at  $2500\text{\AA}$  due to the failure of the mid-UV camera during the UIT *Astro* – 2 mission.) If we assume that galaxy morphology at  $2500\text{\AA}$  is intermediate between that at  $U$ -band and FUV (see also the mid-UV images in Marcum et al. 1997, 2000), we can expect that their  $A$ – $C$  locus would be in the upper left part of the HDF region, between our  $z \sim 1.2$  and  $z \sim 3$  simulations. Abraham et al. interpret the HDF galaxies that lie outside the locus of artificially redshifted Frei data as either very late Hubble types, spirals that have evolved since this look-back time, or mergers/peculiar galaxies. However, the presence of several of our simulated  $z \sim 3$  points within that part of the shaded HDF locus may suggest that these HDF galaxies have  $z \geq 3$  and are being sampled in their rest-frame UV even on the F814W images. Our sample size is insufficient to speculate on what fraction of high-redshift peculiar galaxies might be similar to local spirals, but our FUV  $C$  and  $A$  measurements demonstrate that it is certainly possible to reproduce examples of the apparent peculiar HDF objects without necessarily invoking dramatic evolution.

Our artificially redshifted FUV galaxy images also provide qualitative support for the idea that bandshifting and distance effects alone are capable of producing the morphologies observed in high-redshift galaxies. The top left panel of Figure 13 shows the Sab galaxy NCG 1068 as it would be observed at  $z \sim 4$ . Its FUV-bright starburst + AGN center gives the appearance of a compact core surrounded by diffuse light. This morphology is strikingly similar to that observed by Giavalisco, Steidel, & Duccio Macchetto (1996b) in many Lyman-break galaxies, and the approximate radius of the NGC 1068 core at this redshift ( $\sim 0.4$  arcsec) is comparable to their core radii. The highly inclined Sd galaxy NGC 4631, when observed at  $z \sim 3$ , (see Figure 13), bears a strong resemblance to the “chain galaxies” presented in Figure 20 of Cowie, Hu, & Songaila (1995). We estimate an FUV axial ratio of  $\sim 5$  for this galaxy based on ellipse fitting to the rest-frame image, which is near the middle of the range quoted by Cowie et al. At increasing redshift, surface brightness effects cause the galaxy to appear even thinner and produce the appearance of discrete star-forming



regions “chained” together. The FUV images of NGC 4631 support the interpretations of Dalcanton & Schectman (1996), van den Bergh et al. (1996), and Smith et al. (1997) that the “chain galaxies” are in fact edge-on disks. Other peculiar galaxy types noted in the HDF by van den Bergh et al. are the “tadpole” (head-tail) galaxies and several examples of multiple mergers (see also Pascarelle et al. 1996 for a discussion of the mergers of compact objects). At  $z \sim 3$ , the Sd galaxy NGC 1313 (also shown in Figure 13) could easily be mistaken for the type of merger of compact objects depicted in Figure 4 of van den Bergh et al. Bright inner star-forming regions in NGC 4258 (lower right panel of Figure 13) give the galaxy a “tadpole” appearance at  $z \sim 2$ , similar to the object in Figure 2 of van den Bergh et al. NGC 4258 could also be interpreted as a multiple merger on the basis of several components visible in the image. Along with the irregular/peculiar  $A - C$  classifications of our artificially redshifted galaxy images, the individual examples presented here suggest that one must approach with extreme caution the interpretation of morphology in deep surveys.

The issue of what fraction of high-redshift galaxies have structure similar to local spirals rather than intrinsically irregular morphologies bears strongly on inferences of evolution in the galaxy population. If the absence of “ordered” spirals at  $z > 2$  noted by Driver et al. (1998) is in part due to bandshifting effects, their suggestion that the disk formation epoch occurs at  $z \sim 2$  may need to be modified. Similarly, some of the compact objects at  $z > 3$  may be the UV-bright cores of existing disk galaxies rather than the early progenitors of spheroidal components as hypothesized by Giavalisco et al. (1996b). The apparent peculiarity of high-redshift galaxies has also prompted estimates of high merger rates at  $z > 1.5$  (Driver et al.) and an increased merger fraction with redshift (van den Bergh et al. 1996). However, merger rates at high redshift are particularly difficult to estimate due to the fragmented appearance in the rest-frame UV of even undisturbed galaxies. As noted by Bunker et al. (1999) and Hibbard & Vacca (1997), it is likely that

imaging at longer rest wavelengths will be necessary to determine if there is a regular, underlying structure of older stars in any of the high-redshift galaxies. Alternatively, it would be of interest to obtain a large sample of local UV galaxy images such as that proposed by the Galaxy Evolution Explorer (GALEX, Martin et al. 1999). By comparing the local and distant UV morphologies on a statistical basis, one could infer evolution in the UV properties and thus study the history of physical processes that produce UV emission without reference to the optical light. Although the full picture of evolution would necessarily be incomplete without data for the old stars, an UV database for local galaxies would provide a direct comparison for distant systems.

Our lack of success in classifying FUV galaxies in terms of Hubble types (in this paper and K00) drives us to consider alternate methods of characterizing their morphology. We therefore propose some specific elements of a classification system that would enhance our descriptive power for FUV images and for irregular/peculiar galaxies in general. A new method of defining galaxy apertures that does not assume a generally symmetric distribution around a central brightness enhancement, would greatly extend the capabilities to describe peculiar systems and mergers. In K00, we treat the merger system NGC 4038/9 (the Antennae) as one galaxy and define the aperture to be a circle enclosing all pixels above  $1.5\sigma_{\text{sky}}$  that have at least four adjacent neighbors also above the threshold. A similar procedure could be used to define elliptical apertures for any galaxy. It is also desirable to find parameters that are robust against errors in centroiding: the brightest part of the FUV image is often not at, or even near, the optical center, due to the prominence of off-center star-forming regions. Instead of a *central* concentration measurement, a simple concentration index that measures the fraction of total light in a small aperture around the brightest pixel (wherever it is located) may be more appropriately measured on irregular galaxies. Another useful element would be the scale of various features or asymmetries. This would distinguish between a global disturbance and a peculiarity due to a small, bright

region. One could also measure the size scale of the brightest emitting regions to determine if most of the light comes from one large structure or many smaller ones and thus describe the texture or “patchiness” of the galaxy. Finally, it is important to consider the effects of noise on any derived morphological parameters, especially for rest-frame UV images or faint galaxies. In our FUV images, large regions within the galaxy aperture often contain little or no galaxy light, contributing noise but no signal to the measurements (particularly the asymmetry).

In the future, we intend to develop quantitative morphological parameters applicable to rest-frame UV images, which could serve as tools for morphological analysis of future UV imaging data from STIS and GALEX as well as deep optical/NIR surveys of distant objects. A classification scheme with the characteristics outlined above could prove a valuable addition to the Hubble sequence for studies of evolution in the galaxy population over the history of the universe.

The authors gratefully acknowledge the help of R. Bernstein, J. Parker, R. Phelps, and N. Silbermann for obtaining some of the optical imaging data presented here. We thank O. Pevunova for assistance with preliminary data reduction. Funding for the UIT project was provided through the Spacelab office at NASA Headquarters under Project Number 440-51. WLF and BFM acknowledge support from the Astro-2 Guest Investigator Program through grant number NAG8-1051. Some of the data presented here were obtained at CTIO, which is operated by AURA as part of NOAO under a cooperative agreement with the National Science Foundation. This research has made use of the NASA/IPAC Extragalactic Database (NED), which is operated by the Jet Propulsion Laboratory, California Institute of Technology, under contract with NASA.

## REFERENCES

- Abraham, R. G., Freedman, W. L., & Madore, B. F. 1997, in *HST* and the High Redshift Universe, ed. N. R. Tanvir et al. (Singapore: World Scientific), 57
- Abraham, R. G., Tanvir, N. R., Santiago, B. X., Ellis, R. S., Glazebrook, K. G., & van den Bergh, S. 1996, MNRAS, 279, L47
- Abraham, R. G., Valdes, F., Yee, H. K. C., & van den Bergh, S. 1994, ApJ, 432, 75
- Abraham, R. G., van den Bergh, S., Ellis, R. S., Glazebrook, K., Santiago, B. X., Griffiths, R. E., & Surma, P. 1996, ApJS, 107, 1
- Baugh, C. M., Cole, S., & Frenk, C. S. 1996, MNRAS, 282, L27
- Biretta, J. (ed.) 1996, WFPC2 Instrument Handbook, Version 4.0, Space Telescope Science Institute
- Brinchmann, J. et al. 1998, ApJ, 499, 112
- Bunker, A. J. 1999, to appear in The OCIW Workshop on Photometric Redshifts, ed. Weymann, R., Storrie-Lombardi, L., Sawicki, M., & Brunner, R. (*astro-ph* 9907196)
- Burstein, D., & Heiles, C. 1984, ApJS, 54, 33
- Conselice, C. J. 1997, PASP, 109, 1251
- Conselice, C. J., Bershad, M. A., & Jangren, A. 1999, ApJ, in press (*astro-ph* 9907399)
- Cardelli, J. A., Clayton, G. C., & Mathis, J. S. 1989, ApJ, 345, 245
- Courteau, S., de Jong, R. S., & Broeils, A. H. 1996, ApJ, 457, L73
- Cowie, L. L., Hu, E. M., & Songaila, A. 1995, AJ, 110, 1576

- Dalcanton, J. J., & Schectman, S. A. 1996, *ApJ*, 465, L9
- de Vaucouleurs, G., de Vaucouleurs, A., Corwin, H. G., Buta, R. J., Paturel, G., & Fouqué, P. 1991, *Third Reference Catalogue of Bright Galaxies*, (New York: Springer Verlag) (*RC3*)
- Doi, M., Fukugita, M., & Okamura, S. 1993, *MNRAS*, 164, 832
- Donas, J., Milliard, B., & Laget, M. 1995, *A&A*, 303, 661
- Driver, S. P., Fernandez-Soto, A., Couch, W. J., Odewahn, S. C., Windhorst, R. A., Phillips, S., Lanzetta, K., & Yahil, A. 1998, *ApJ*, 496, L93
- Fanelli, M. N., et al. 1997, in *The Ultraviolet Universe at Low and High Redshift*, ed. W. H. Waller et al. (Woodbury, NY: AIP), 83
- Fanelli, M. N., et al. 1997, *ApJ*, 481, 735
- Ferrarese, L., et al. 1999, in *ASP Conf. Series on Cosmic Flows*, ed. S. Courteau, M. Strauss, & J. Willick
- Frei, Z., Guhathakurta, P., Gunn, J. E., & Tyson, J. A. 1996, *AJ*, 111, 174
- Gardner, J. P., Heap, S. R., Malumuth, E. M., Hill, R. S., & Smith, E. P. 1997, in *The Ultraviolet Universe at Low and High Redshift*, ed. W. H. Waller et al. (Woodbury, NY: AIP), 42
- Giavalisco, M., Livio, M., Bohlin, R. C., Duccio Macchetto, F., & Stecher, T. P. 1996, *AJ*, 112, 369
- Giavalisco, M., Steidel, C. C., & Duccio Macchetto, F. 1996, *ApJ*, 470, 189
- Hibbard, J. E., & Vacca, W. D. 1997, *AJ*, 114, 5

- Kent, S. M. 1986, *AJ*, 91, 1301
- Kormendy, J. 1982, in *Morphology and Dynamics of Galaxies*, ed. L. Martinet & M. Mayor, (Sauverny: Geneva Observatory), 113
- Kuchinski, L. E., et al. 1999, *ApJS*, submitted (K00)
- Marcum, P. M., et al. 2000, in preparation
- Marcum, P. M., et al. 1997, in *The Ultraviolet Universe at Low and High Redshift*, ed. W. H. Waller et al. (Woodbury, NY: AIP), 88
- Martin, C. D., et al. 1999, in *Ultraviolet–Optical Space Astronomy Beyond HST*, ed. J. A. Morse, J. M. Shull, & A. L. Kinney (San Francisco: ASP), 182
- Morgan, W. W. 1958, *PASP*, 70, 364
- Naim, A., & Lahav, O. 1997, *MNRAS*, 286, 969
- Naim, A., Ratnatunga, K. U., & Griffiths, R. E. 1997, *ApJ*, 476, 510
- Naim, A., et al. 1995, *MNRAS*, 274, 1107
- Neff, S. G., Fanelli, M. N., Roberts, L. J., O’Connell, R. W., Bohlin, R. C., Roberts, M. S., Smith, A. M., & Stecher, T. P. 1994, *ApJ*, 430, 545
- O’Connell, R. W. 1999, to appear in *ARA&A*, 1999
- O’Connell, R. W. 1997, in *The Ultraviolet Universe at Low and High Redshift*, ed. W. H. Waller et al. (Woodbury, NY: AIP), 11
- Odewahn, S. C., Windhorst, R. A., Driver, S. P., & Keel, W. C. 1996, *ApJ*, 472, L13
- Okamura, S., Kodaira, K., & Watanabe, M. 1984, *ApJ*, 280, 7

- Pascarelle, S. M., Windhorst, R. A., Keel, W. C., & Odewahn, S. C. 1996, *Nature*, 383, 45
- Pfenniger, D., & Norman, C. 1990, *ApJ*, 363, 391
- Roberts, M. S., & Haynes, M. P. 1994, *ARA&A*, 32, 115
- Smith, A. M., Collins, N. R., Waller, W. H., Fanelli, M. N., Stecher, T. P., & the UIT Team  
1997, in *The Ultraviolet Universe at Low and High Redshift*, ed. W. H. Waller et  
al. (Woodbury, NY: AIP), 439
- Smith, D. A., et al. 1996, *ApJ*, 473, L21
- Stecher, T. P., et al. 1997, *PASP*, 109, 58, 4
- Stover, R. J. 1988, in *Instrumentation for Ground-Based Optical Astronomy*, ed. L. B.  
Robinson (New York: Springer), 443
- Teplitz, H. I., Gardner, J. P., Malumuth, E. M., & Heap, S. R. 1998, *ApJ*, 507, L17
- Tody, D. 1986, *SPIE*, 627, 733
- Tully, R. B. 1988, *Catalog of Nearby Galaxies*, (Cambridge: Cambridge UP)
- van den Bergh, S., Abraham, R. G., Ellis, R. S., Tanvir, N. R., Santiago, B. X., &  
Glazebrook, K. G. 1996, *AJ*, 112, 359
- Voit, M. (ed.) 1997, *HST Data Handbook Version 3.0, Volume I*
- Waller, W. H., Fanelli, M. N., Collins, N. R., Cornett, R. H., Offenberg, J., Marcum, P. M.,  
Stecher, T. P., & the UIT Science Team, in *The Ultraviolet Universe at Low and  
High Redshift*, ed. W. H. Waller et al. (Woodbury, NY: AIP), 39
- Williams, R. E., et al. 1996, *AJ*, 112, 1335

Fig. 1.— FUV and artificially redshifted images of M101 and NGC 4214, oriented with North up and East to the left. The FUV M101 image is a 1311s UIT exposure, and the redshifted M101 images are scaled as they would appear in the HDF. The FUV NGC 4214 image is a 1061s UIT exposure, and the redshifted NGC 4214 images again simulate the HDF. The scale bar shown in the F300W panel for each galaxy is applicable to all redshifted images of that galaxy.

Fig. 2.—  $U$ -band and artificially redshifted images of M51, oriented with North up and East to the left. The  $U$ -band image has foreground stars removed. The center and right-hand panels and simulate the appearance of M51 in the HDF at the redshifts noted on the labels.

Fig. 3.— Values of the central concentration ( $C$ ) and asymmetry ( $A$ ) indices as a function of wavelength for ten galaxies in our sample.

Fig. 4.— Change in  $C$  and  $A$  between optical and FUV images, for different optical filters noted on the label in each panel. Open circles are galaxies of type E/S0, solid squares are types Sa–Sb, open squares are Sbc–Sd, and stars are types Irr/Pec/Merger. Errorbars for  $\Delta C$  and  $\Delta A$  are shown in the bottom panels. In the right-hand panels, solid horizontal lines mark  $\Delta C, A = 0$ , diagonal dotted lines are fits to data from all filters together, and diagonal solid lines are fits to data for each filter individually.

Fig. 5.— Optical and FUV images of NGC 1512, NGC 3310, and NGC 4736 to demonstrate band-shifting effects in various galaxy types. Images are registered to the FUV coordinate system and oriented with North up and East to the left. As in K00, images are displayed in calibrated flux units such that pixels of the same surface brightness have constant darkness for both images of the same galaxy. The scale bar in the lower right is applicable to all images.



Fig. 6.— Optical ( $V$  or  $R$  as available,  $B$  for NGC 1068) and FUV galaxy data on the  $\log C$  vs  $\log A$  diagram. Symbols for galaxies of different Hubble types are the same as in Figure 4. Dashed lines denote the divisions into morphological bins used by Abraham et al.(1996b), which have been shifted by the offsets calculated in Section 3. Errorbars for different locations on the diagram are shown as described in the text.

Fig. 7.— Histograms of the change in  $C$  and  $A$  between the  $U$ -band or FUV image and its artificially redshifted counterparts. The bin size is 0.1, and errorbars for  $\Delta C$  and  $\Delta A$  based on the uncertainties in  $C$  and  $A$  (see text) are shown in the top panels. Labels in each panel show the rest-frame image used (either  $U$  or FUV) and the redshift simulated.

Fig. 8.— Histograms of  $\Delta C$  and  $\Delta A$  resulting from changing the aperture size from a fixed limit for all data to an adjusted value based on the limiting surface brightness of each image. Errorbars are shown based on the propagation of our uncertainties in  $C$  and  $A$  through the arithmetic to get  $\Delta C, A$ . This likely overestimates the true error, as here we are comparing values of  $C, A$  measured on the same image but with different aperture radii.

Fig. 9.— The apparent change in galaxy morphology with redshift in optical observations. The left-hand panels show nearby galaxies as seen in the  $V$ -band, the center and right-hand panels show the same galaxies as they would appear at the redshifts and in the WFPC2 filters noted on the labels. The center panels are artificially redshifted rest-frame  $U$ -band images, and the right-hand panels are rest-frame FUV images. Each  $V$ -band image is scaled to the equivalent of a  $\sim 5$  second exposure and binned by 3; the artificially redshifted images are unbinned and represent  $\sim 5\%$  of the HDF exposure time for the center panels and the entire HDF exposure time for the right-hand panels.

Fig. 10.— The change in locus of galaxies on the  $\log C$  vs  $\log A$  diagram with redshift. Symbols for galaxies of different Hubble types are the same as in Figure 4, and dashed lines

denote the divisions into morphological bins as in Figure 6. Representative errorbars for different locations on the diagram are shown in the final panel, as in Figure 6. Data for  $z \leq 1.2$  are from redshift simulations of rest-frame  $U$ -band images, and data for  $z \geq 2$  are from artificially redshifted FUV images.

Fig. 11.— Trajectories of several galaxies in the  $\log C$  vs  $\log A$  diagram from their position as measured on optical images to that measured on artificially redshifted rest-frame UV images. The larger point for each galaxy marks the optical position, then smaller points at each simulated redshift are connected in order by the lines.

Fig. 12.— Comparison to the HDF morphologies and redshift simulations of Abraham et al. (1996a). The shaded region denotes the area occupied by HDF galaxies, and the open polygon is the locus of the artificially redshifted Frei galaxy sample as measured by Abraham et al. (1996a). Our data for different redshift simulations are shown as different symbols for each redshift, as noted on the plot. Errorbars for different locations on the diagram are shown.

Fig. 13.— Simulated high-redshift spirals that resemble peculiar galaxy types identified in deep survey images. Images are oriented with North up and East to the left, and a scale bar and label for the simulated redshift are shown in each panel.

TABLE 1  
BASIC DATA FOR SAMPLE GALAXIES WITH FUV IMAGES

Name	Hubble Type <sup>a</sup>	Optical Data <sup>b</sup>	Redshifted FUV <sup>b</sup>	Redshifted $U^b$
NGC 925	SAB(s)d	<i>UBVR</i>	Y	Y
NGC 1068 (M77)	RSA(rs)b	<i>UB</i>	Y	Y
NGC 1097	SB(s)b	<i>UBVI</i>	Y	Y
NGC 1313	SB(s)d	<i>UBVI</i>	Y	Y
NGC 1365	SB(s)b	...	Y	N
NGC 1510	S0 pec	<i>UBVI</i>	N	N
NGC 1512	SB(r)a	<i>UBVI</i>	Y	Y
NGC 1566	SAB(s)bc	<i>UBVI</i>	Y	Y
NGC 1672	SB(s)b	<i>UBVI</i>	Y	Y
NGC 2403	SAB(s)cd	<i>UBVRI</i>	Y	Y
NGC 2841	SA(r)b	<i>UVR</i>	N	Y
NGC 2903	SAB(rs)bc	<i>UBVR</i>	Y	Y
NGC 3226	E2 pec	<i>BR</i>	Y	N
NGC 3227	SAB(s)a pec	<i>BR</i>	Y	N
NGC 3310	SAB(r)bc pec	<i>VR</i>	Y	N
NGC 3351 (M95)	SB(r)b	<i>BVRI</i>	N	N
NGC 3389	SA(s)c	<i>R</i>	Y	N
NGC 4038	SB(s)m pec	<i>UVI</i>	Y	Y
NGC 4039	SA(s)m pec	<i>UVI</i>	Y	Y
NGC 4214	IAB(s)m	<i>BVRI</i>	Y	N
NGC 4258 (M106)	SAB(s)bc	...	Y	N
NGC 4449	IBm	<i>BVRI</i>	Y	N
NGC 4470	Sa pec	...	Y	N
NGC 4486 (M 87)	E0 pec (cD)	...	Y	N
NGC 4631	SB(s)d	...	Y	N
NGC 4647	SAB(rs)c	<i>R</i>	N	N
NGC 4736 (M94)	(R)SA(r)ab	<i>UV</i>	Y	Y
NGC 5055 (M63)	SA(rs)bc	<i>UBVR</i>	N	Y
NGC 5194 (M51)	SA(s)bc pec	<i>UBVRI</i>	Y	Y
NGC 5236 (M83)	SAB(s)c	<i>UBRI</i>	Y	Y
NGC 5253	pec	<i>BVI</i>	N	N
NGC 5457 (M101)	SAB(rs)cd	...	Y	N

<sup>a</sup>Data from the *RC3* (de Vaucouleurs et al. 1991).

<sup>b</sup>Availability of central concentration and asymmetry data, denoted by filter for the FUV/optical column and by Y(es) or N(o) for the redshift simulations.

TABLE 2  
CONCENTRATION AND ASYMMETRY PARAMETERS FOR FUV AND OPTICAL IMAGES

Name	$\epsilon^a$	P.A. <sup>b</sup>	$C_{\text{FUV}}$	$C_U$	$C_B$	$C_V$	$C_R$	$C_I$	$A_{\text{FUV}}$	$A_U$	$A_B$	$A_V$	$A_R$	$A_I$
NGC 925	0.40	115	0.20	0.34	0.37	0.37	0.35	...	0.72	0.22	0.17	0.13	0.15	...
NGC 1068	0.20	84	0.54	0.49	0.50	...	...	...	0.28	0.18	0.13	...	...	...
NGC 1097	0.32	140	0.17	0.44	0.47	0.50	...	0.53	0.64	0.27	0.21	0.19	...	0.12
NGC 1313	0.20	40	0.28	0.39	0.41	0.41	...	0.37	0.64	0.34	0.22	0.21	...	0.17
NGC 1365	0.45	32	0.13	...	...	...	...	...	0.72	...	...	...	...	...
NGC 1510	0.12	145	0.51	0.73	0.68	0.64	...	0.50	0.25	0.21	0.16	0.15	...	0.10
NGC 1512	0.36	46	0.15	0.34	0.37	0.40	...	0.41	0.69	0.12	0.08	0.06	...	0.04
NGC 1566	0.21	40	0.30	0.54	0.57	0.60	...	0.60	0.47	0.25	0.18	0.15	...	0.12
NGC 1672	0.13	161	0.19	0.35	0.36	0.39	...	0.42	0.61	0.27	0.21	0.17	...	0.11
NGC 2403	0.44	130	0.28	0.41	0.41	0.42	0.45	0.39	0.74	0.26	0.17	0.13	0.14	0.15
NGC 2841	0.56	147	0.14	0.32	...	0.39	0.39	...	0.78	0.12	...	0.10	0.08	...
NGC 2903	0.53	24	0.23	0.32	0.33	0.34	0.35	0.34	0.62	0.16	0.13	0.11	0.10	0.06
NGC 3226/7	0.55	157	0.19	...	0.30	...	0.34	...	0.60	...	0.34	...	0.33	...
NGC 3310	0.22	170	0.76	...	...	0.75	0.73	...	0.17	...	...	0.16	0.12	...
NGC 3351	0.32	17	0.21	...	0.35	0.39	0.40	0.43	0.42	...	0.06	0.05	0.05	0.06
NGC 3389	0.55	108	0.21	...	...	...	0.31	...	0.39	...	...	...	0.19	...
NGC 4038/9	0.00	...	0.14	0.18	...	0.18	...	0.20	0.89	0.63	...	0.48	...	0.42
NGC 4214	0.18	132	0.54	...	0.53	0.54	0.51	0.50	0.35	...	0.14	0.14	0.12	0.13
NGC 4258	0.65	150	0.72	...	...	...	...	...	0.58	...	...	...	...	...
NGC 4449	0.36	60	0.51	...	0.55	0.54	0.51	0.51	0.38	...	0.19	0.17	0.15	0.13
NGC 4470	0.30	0	0.33	...	...	...	...	...	0.20	...	...	...	...	...
NGC 4486	0.10	0	0.39	...	...	...	...	...	0.30	...	...	...	...	...
NGC 4631	0.80	86	0.37	...	...	...	...	...	0.46	...	...	...	...	...
NGC 4647	0.20	135	0.22	...	...	...	0.23	...	0.55	...	...	...	0.11	...
NGC 4736	0.22	95	0.54	0.58	...	0.60	...	...	0.20	0.10	...	0.06	...	...
NGC 5055	0.47	102	0.25	0.38	0.41	0.42	0.43	...	0.59	0.19	0.19	0.17	0.15	...
NGC 5194	0.30	30	0.22	0.30	0.28	0.30	0.30	0.31	0.54	0.30	0.24	0.25	0.24	0.25
NGC 5236	0.10	80	0.23	0.25	0.27	...	0.31	0.36	0.55	0.18	0.21	...	0.13	0.11
NGC 5253	0.57	43	0.66	...	0.50	0.48	...	0.37	0.22	...	0.10	0.12	...	0.08
NGC 5457	0.00	...	0.41	...	...	...	...	...	0.69	...	...	...	...	...

<sup>a</sup>Ellipticity of the galaxy aperture, measured from longest wavelength optical image.

<sup>b</sup>Position angle of the adopted elliptical aperture in degrees. 0° is North, angle increasing to the East.

TABLE 3  
CONCENTRATION AND ASYMMETRY PARAMETERS FOR ARTIFICIALLY REDSHIFTED IMAGES<sup>a</sup>

Name	$C$ (FUV, $z1$ ) <sup>b</sup> $A$		$C$ (FUV, $z2$ ) $A$		$C$ (FUV, $z3$ ) $A$		$C$ (FUV, $z4$ ) $A$		$C$ ( $U$ , $z0.6$ ) $A$		$C$ ( $U$ , $z1.2$ ) $A$	
NGC 925	0.23	0.56	0.22	0.56	0.22	0.52	...	...	0.47	0.24	0.40	0.36
NGC 1068	0.53	0.14	0.51	0.21	0.52	0.20	0.45	0.34	0.38	0.52	0.40	0.54
NGC 1097	0.18	0.55	0.18	0.58	0.18	0.56	0.12	0.66	0.44	0.24	0.42	0.36
NGC 1313	0.35	0.36	0.33	0.36	0.32	0.40	0.17	0.65	0.44	0.36	0.40	0.43
NGC 1365	0.14	0.58	0.14	0.60	0.14	0.57	0.10	0.68	...	...	...	...
NGC 1512	0.18	0.49	0.19	0.49	0.17	0.53	...	...	0.40	0.12	0.35	0.25
NGC 1566	0.31	0.42	0.28	0.47	0.29	0.43	0.15	0.62	0.55	0.25	0.46	0.28
NGC 1672	0.22	0.42	0.22	0.46	0.23	0.45	0.15	0.60	0.43	0.28	0.36	0.30
NGC 2403	0.24	0.58	0.20	0.59	0.20	0.54	...	...	0.44	0.16	0.42	0.20
NGC 2841	...	...	...	...	...	...	...	...	0.33	0.10	0.30	0.09
NGC 2903	0.21	0.50	0.22	0.56	0.21	0.62	...	...	0.31	0.07	0.32	0.06
NGC 3226/7	0.17	0.66	0.15	0.67	0.16	0.66	...	...	...	...	...	...
NGC 3310	0.72	0.26	0.71	0.15	0.72	0.23	0.47	0.18	...	...	...	...
NGC 3389	0.22	0.38	0.21	0.40	0.21	0.38	...	...	...	...	...	...
NGC 4038/9	0.14	0.82	0.13	0.81	0.14	0.80	0.11	0.72	0.23	0.62	0.19	0.62
NGC 4214	0.54	0.18	0.50	0.27	0.52	0.32	0.39	0.48	...	...	...	...
NGC 4258	0.28	0.62	0.25	0.55	0.26	0.561	...	...	...	...	...	...
NGC 4449	0.56	0.15	0.54	0.19	0.51	0.42	0.40	0.31	...	...	...	...
NGC 4470	0.32	0.25	0.33	0.27	0.29	0.27	...	...	...	...	...	...
NGC 4486	0.28	0.42	0.29	0.40	0.33	0.36	...	...	...	...	...	...
NGC 4631	0.33	0.46	0.32	0.42	0.31	0.41	0.21	0.47	...	...	...	...
NGC 4736	0.40	0.19	0.37	0.13	0.37	0.12	0.22	0.38	0.59	0.06	0.54	0.16
NGC 5055	...	...	...	...	...	...	...	...	0.36	0.16	0.39	0.16
NGC 5194	0.15	0.53	0.15	0.54	0.14	0.54	...	...	0.32	0.25	0.31	0.26
NGC 5236	0.18	0.47	0.19	0.52	0.19	0.48	0.16	0.59	0.29	0.19	0.28	0.17
NGC 5457	0.16	0.72	0.14	0.72	0.14	0.68	...	...	...	...	...	...

<sup>a</sup> $C$ ,  $A$  for apertures adjusted to match the limiting surface brightness for each image.

<sup>b</sup> $C$ ,  $A$  for FUV data artificially redshifted to  $z \sim 1$ , other column heads are similar format for FUV or  $U$ -band data artificially redshifted to various  $z$  to match the HDF filters.

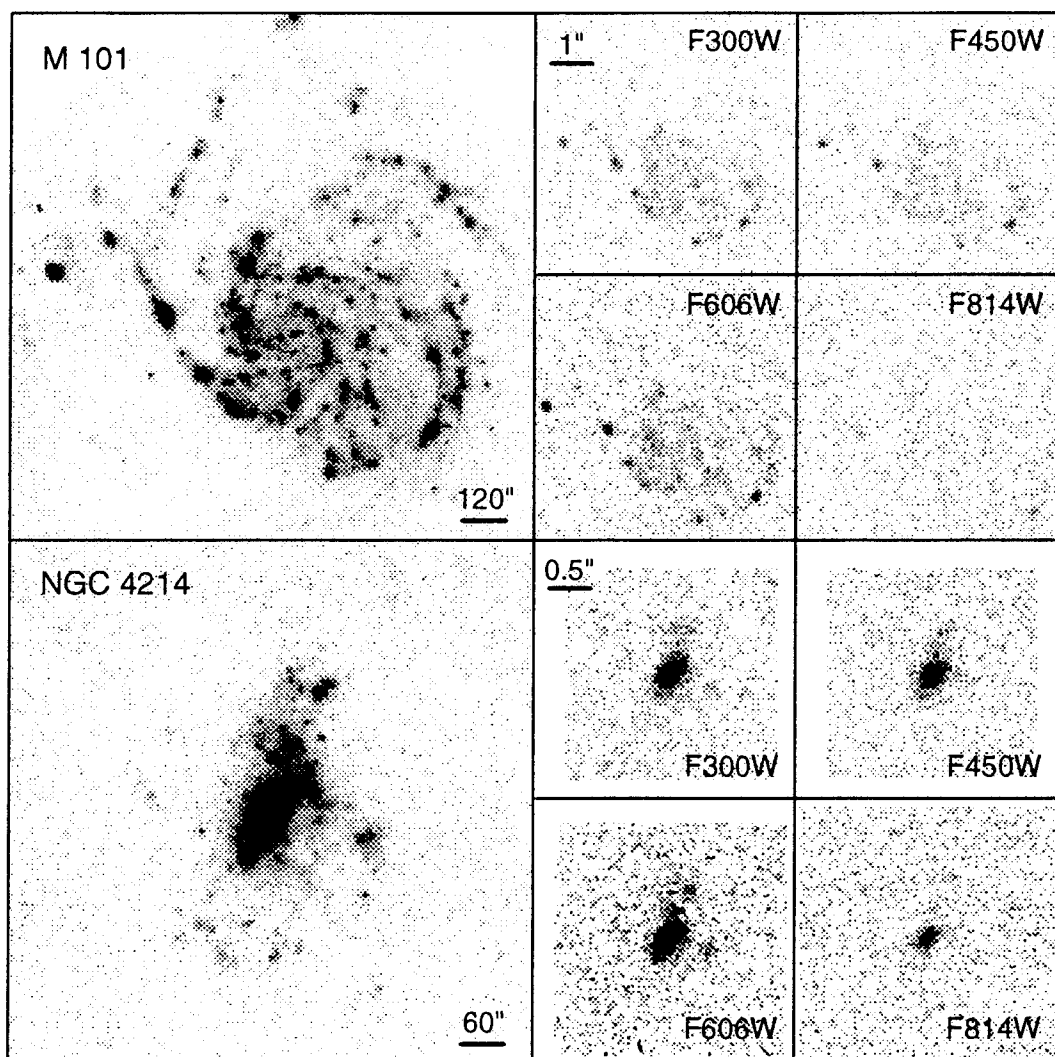


Fig. 1.—

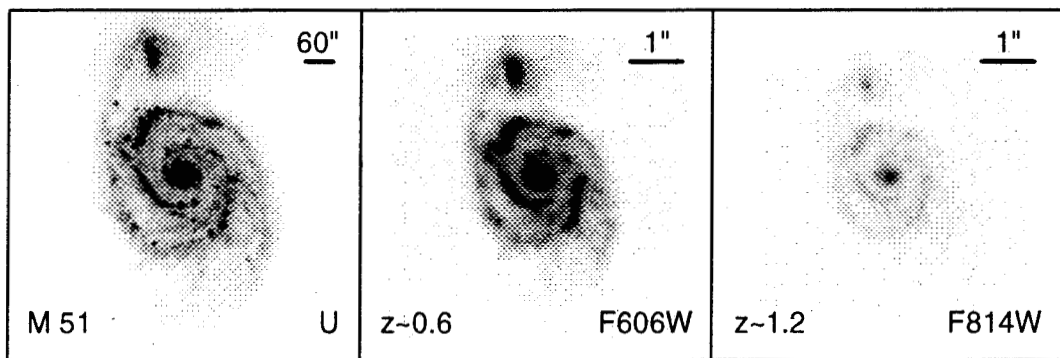


Fig. 2.—

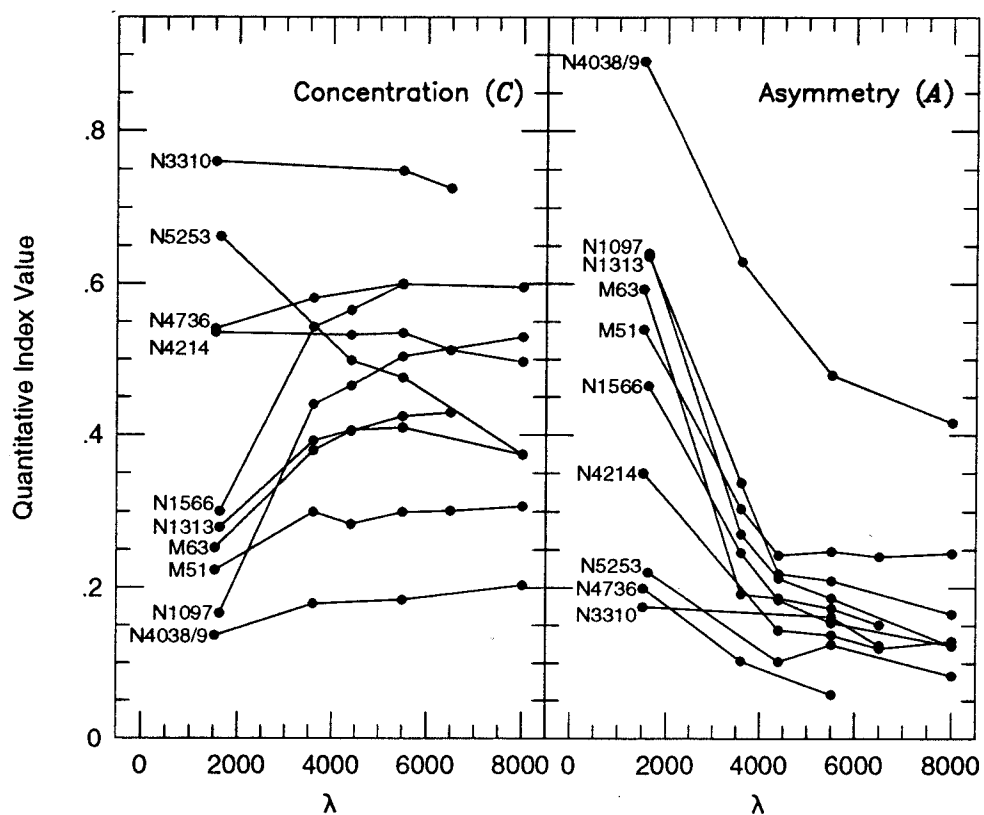


Fig. 3.—



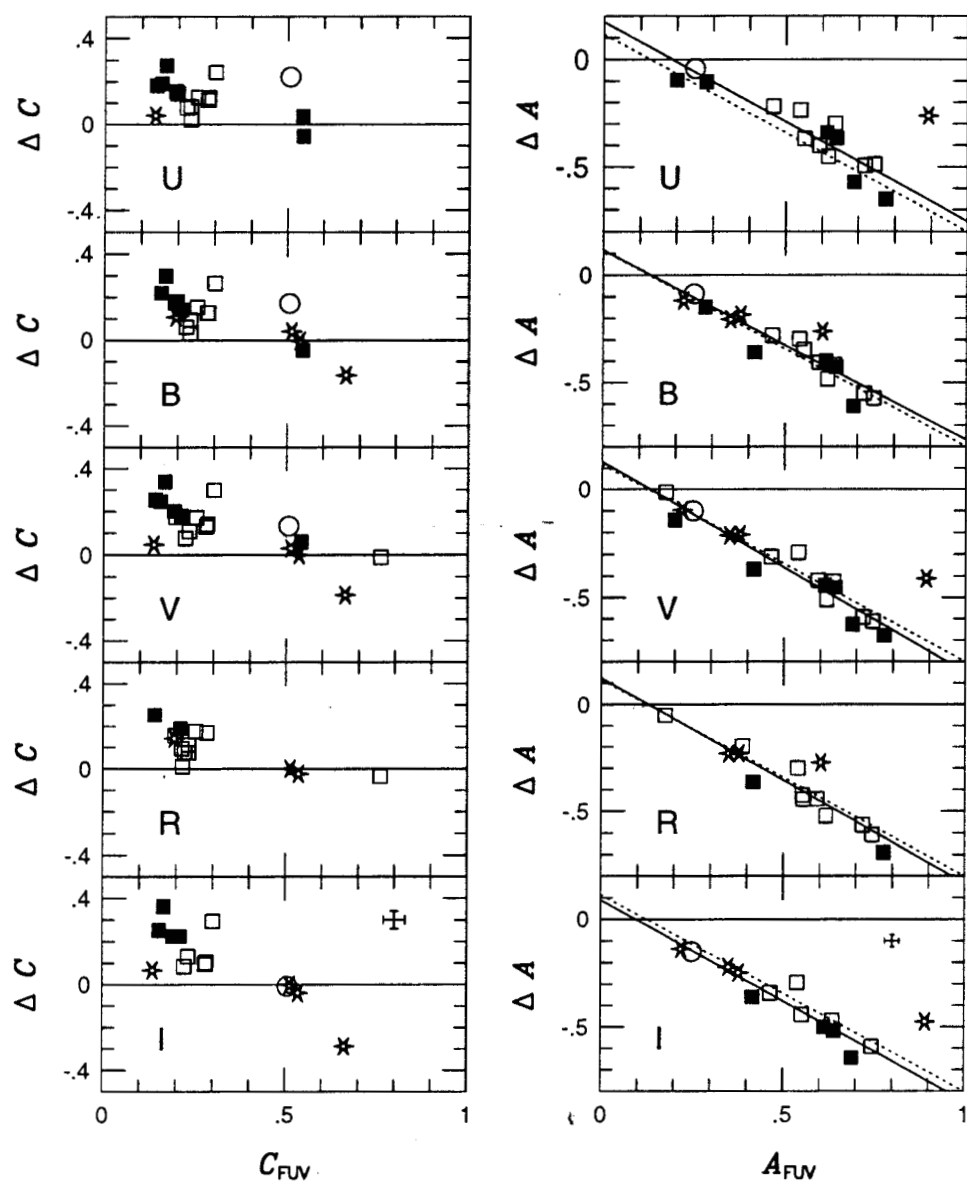


Fig. 4.—

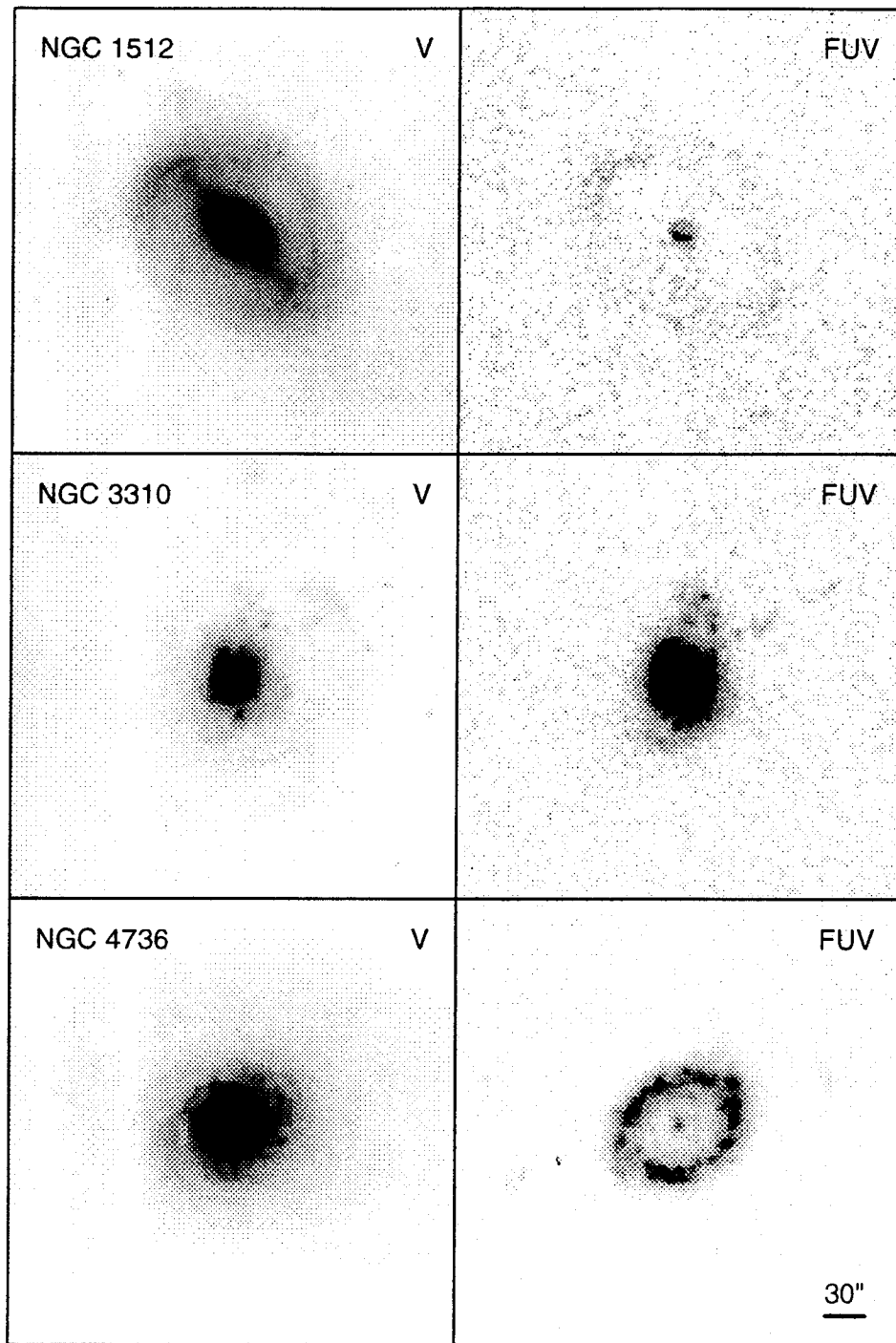


Fig. 5.—

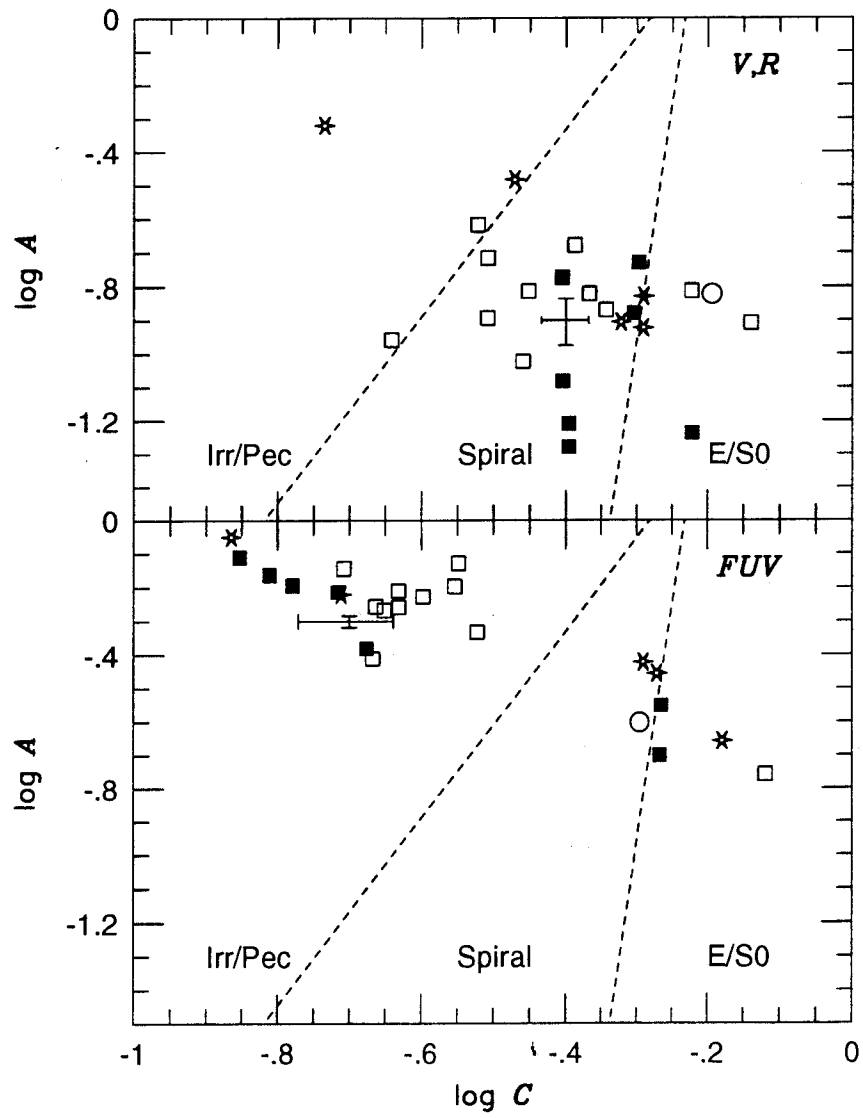


Fig. 6.—

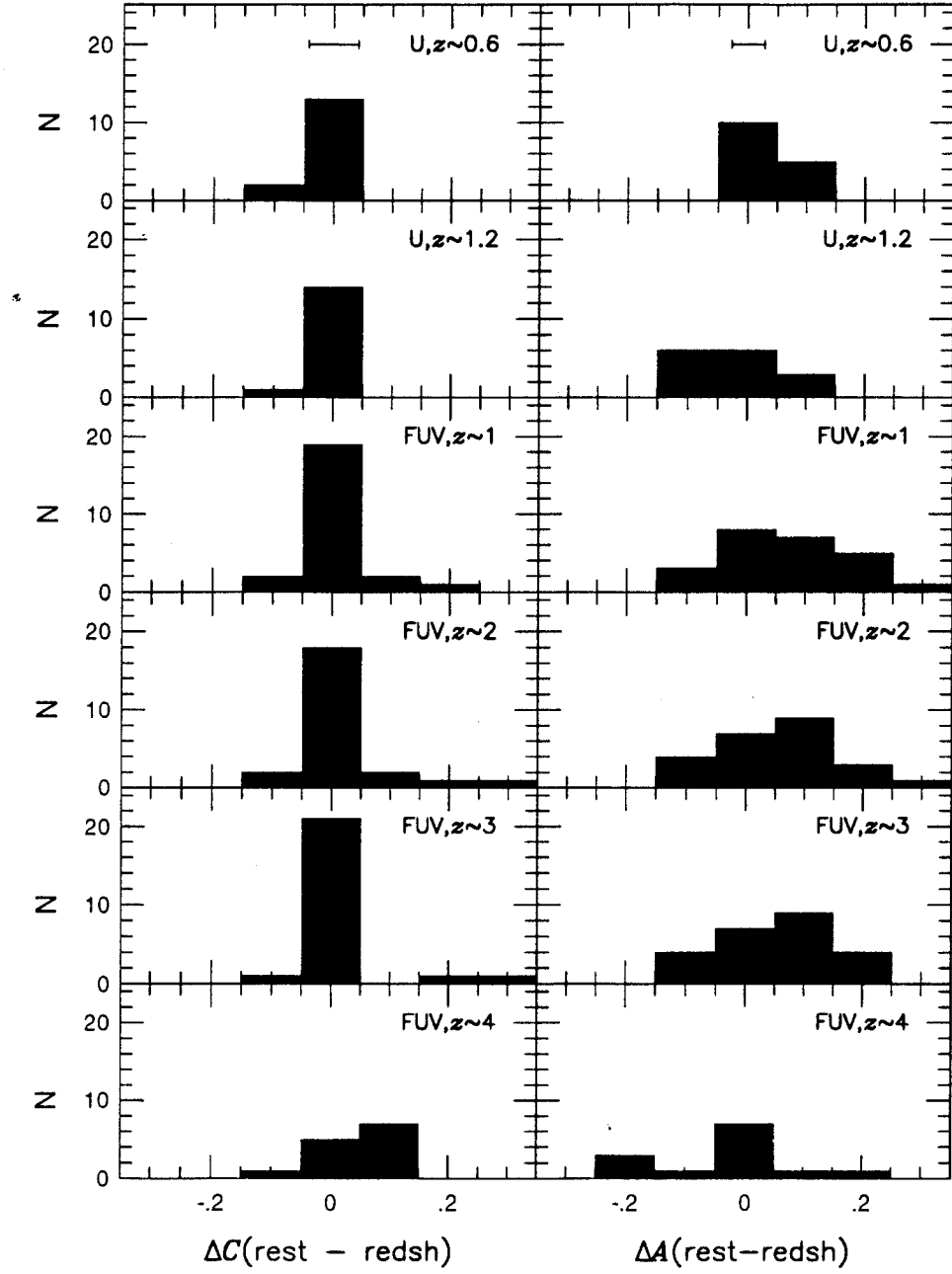


Fig. 7.—

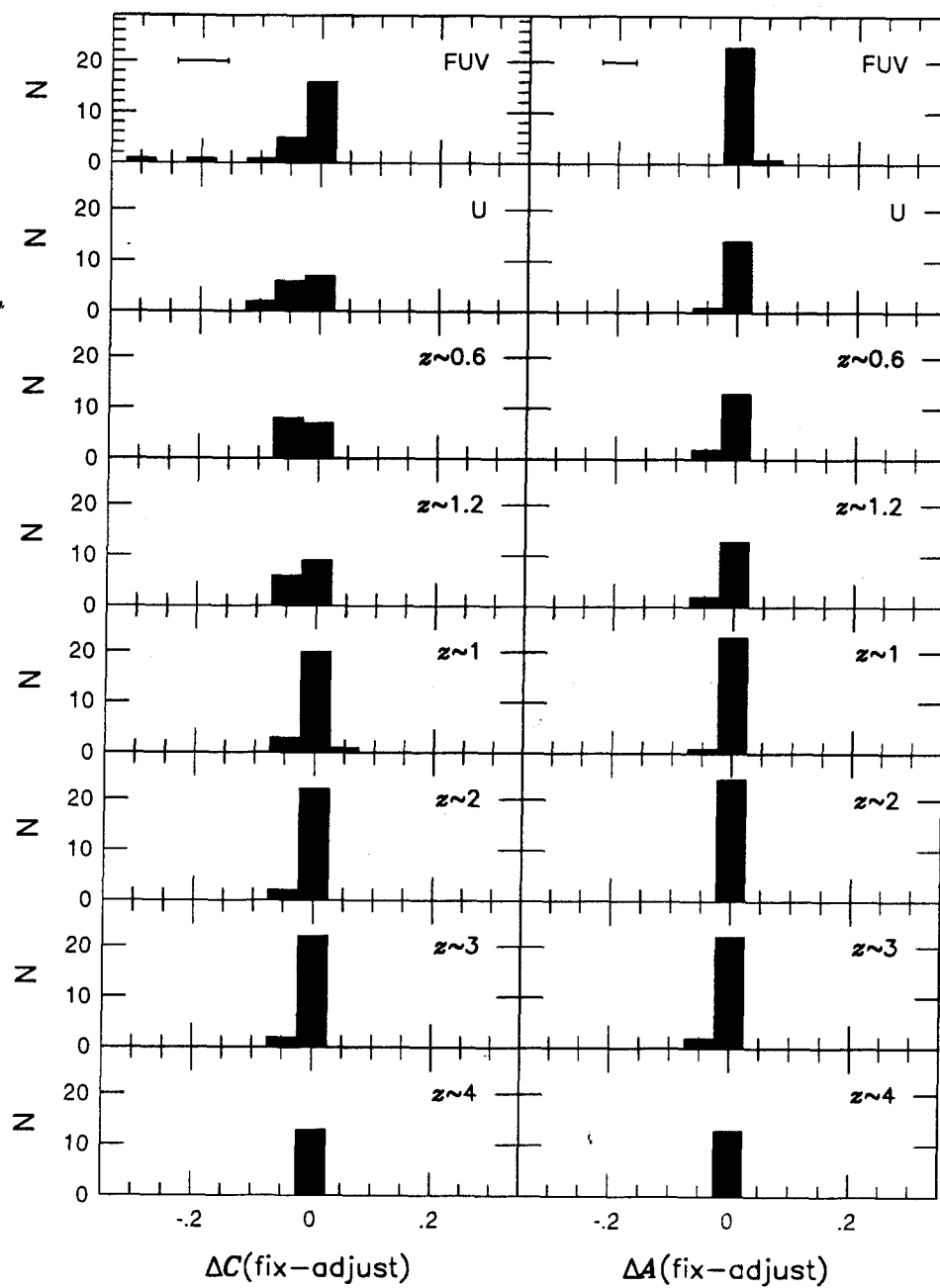


Fig. 8.—

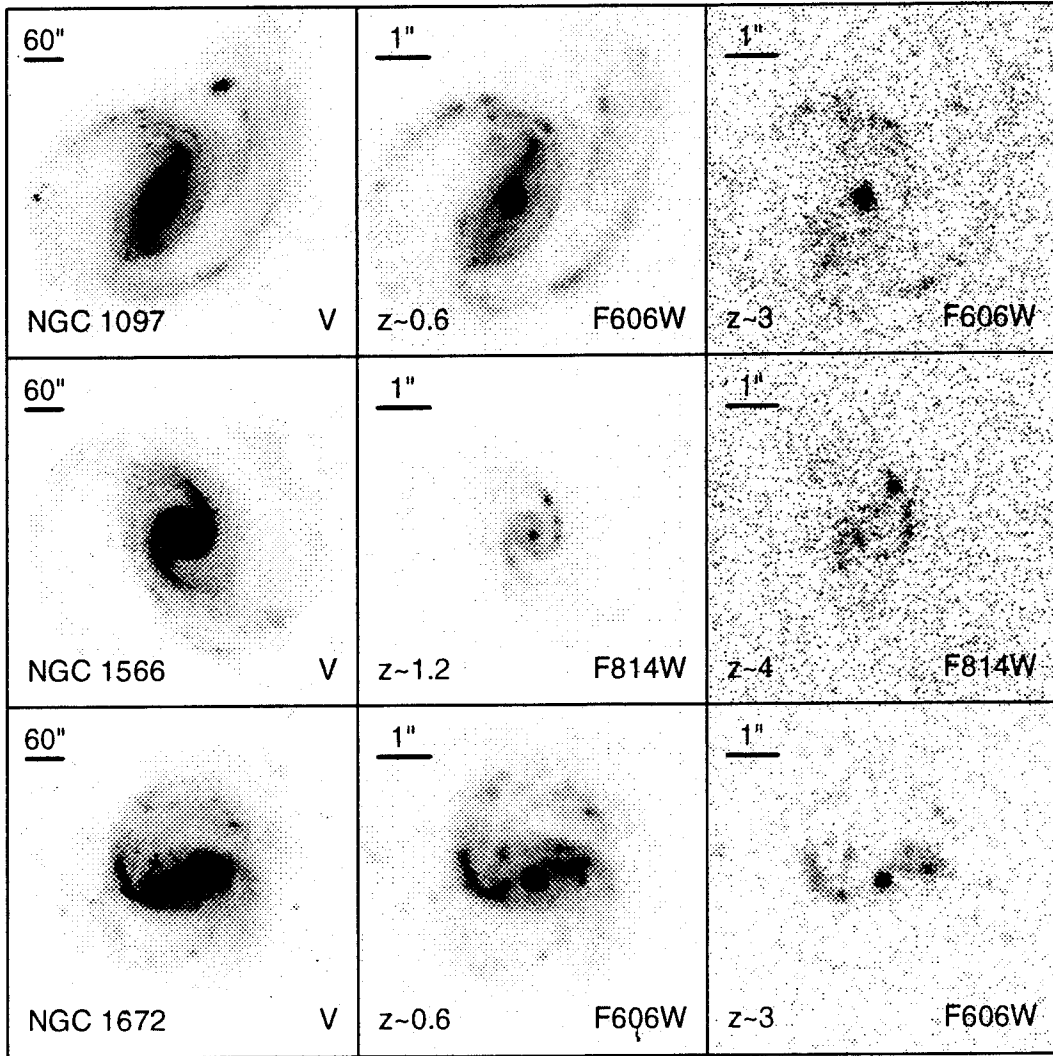


Fig. 9.—

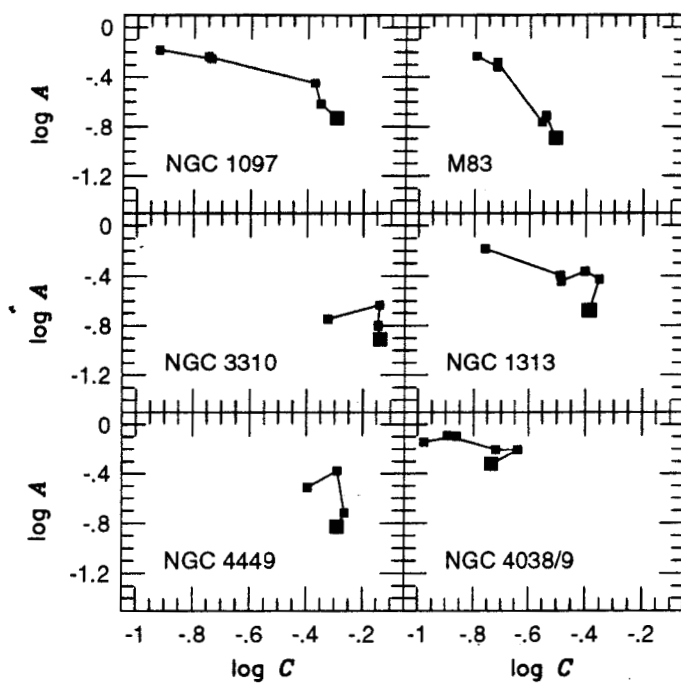


Fig. 11.—

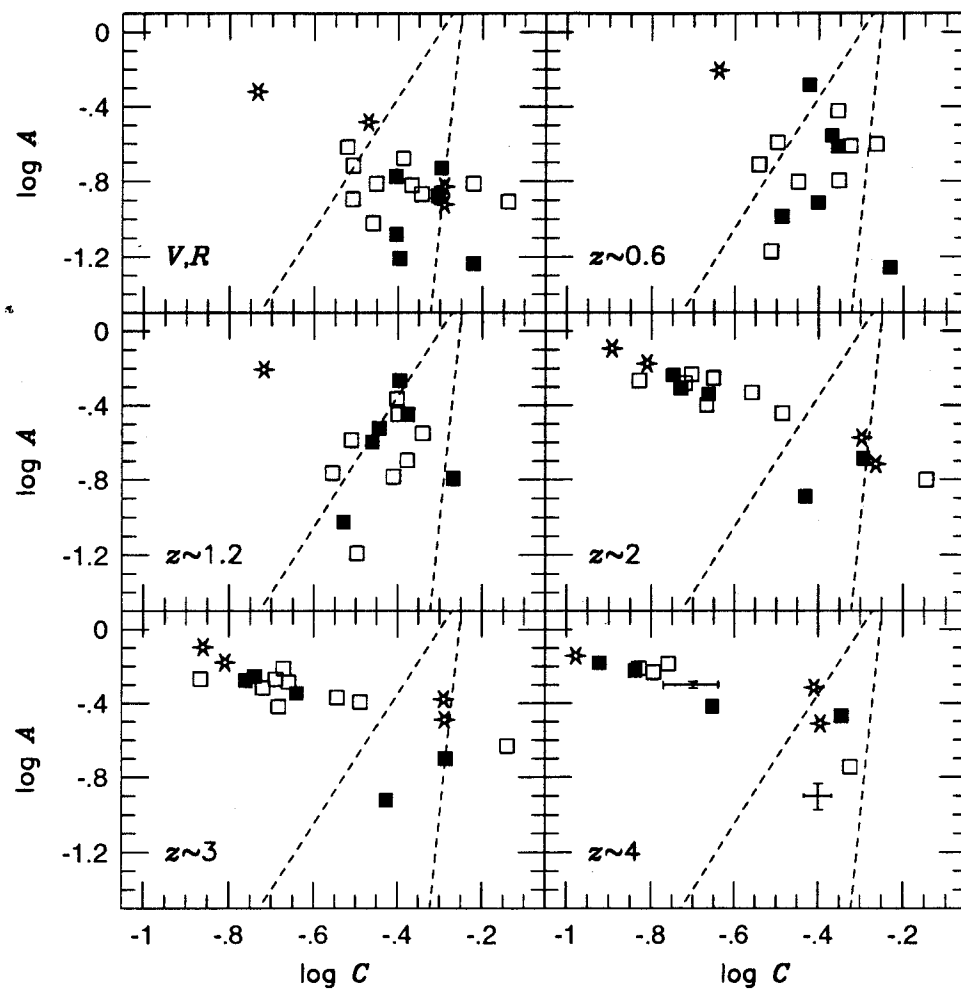


Fig. 10.—



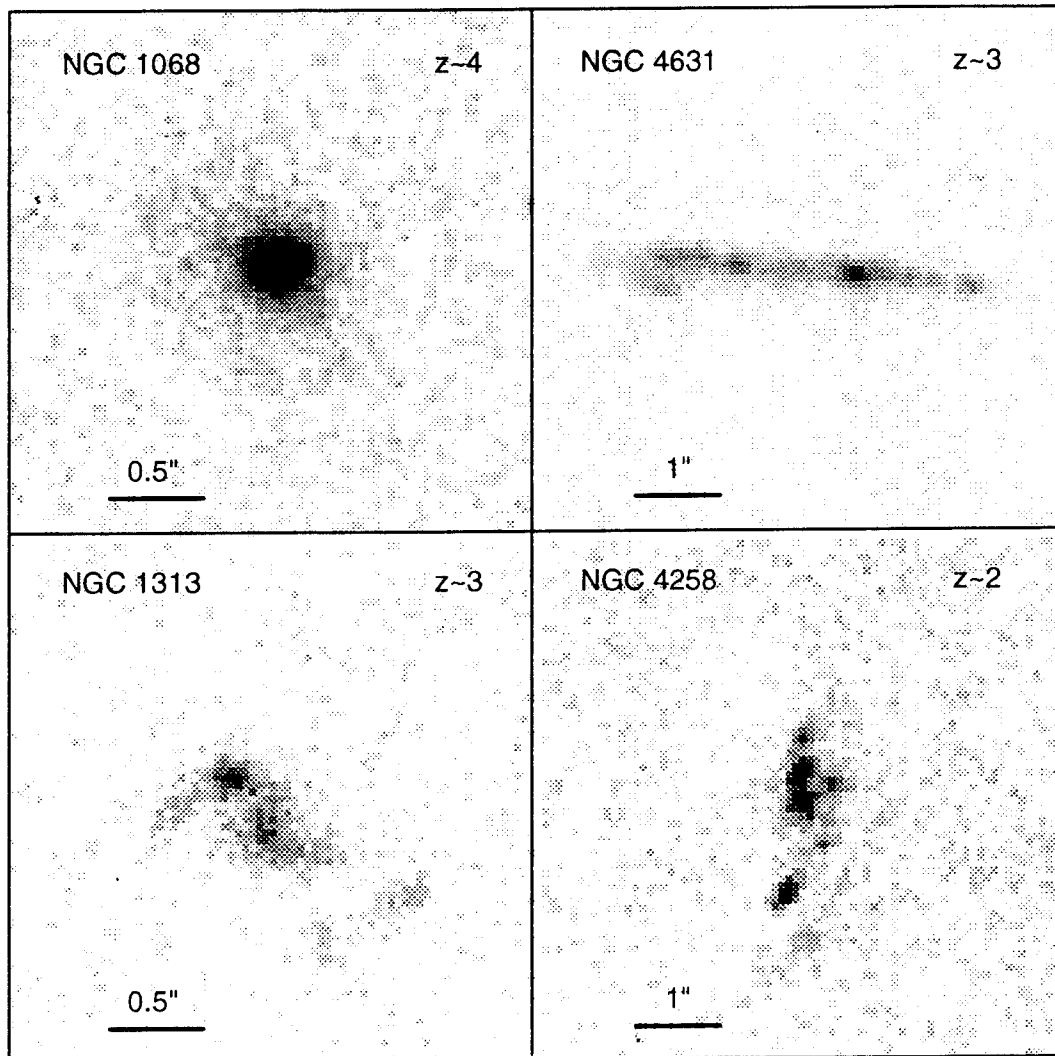


Fig. 13.—

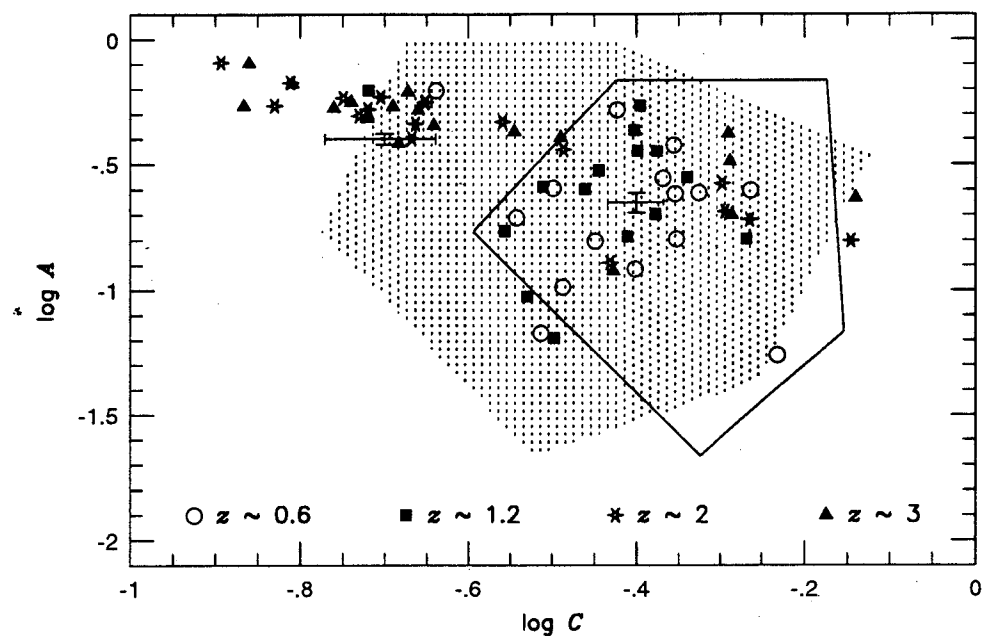


Fig. 12.—